Epigenome and transcriptome landscapes highlight dual roles of proinflammatory players in a perinatal model of white matter injury

Anne-Laure SCHANG[1,2,3,4,*], Juliette van STEENWINCKEL[3,4,†], Julia LIPECKI[6,†], Charlotte RICH-GRIFFIN[6], Kate WOOLLEY-ALLEN[6], Nigel DYER[5], Tifenn Le CHARPENTIER[3,4], Patrick SCHÄFER[6], Bobbi FLEISS[3,4,7], Sascha OTT[5,‡,§], Délara SABÉRAN-DJONEIDI[1,2,3,‡,§], Valérie MEZGER[1,2,3,‡, §], Pierre GRESSENS[3,4,7,‡]

[1] CNRS, UMR7216 Épigénétique et Destin Cellulaire, F-75205 Paris Cedex 13, France
[2] Univ Paris Diderot, Sorbonne Paris Cité, F-75205 Paris Cedex 13, France
[3] Département Hospitalo-Universitaire DHU PROTECT, Paris, France
[4] NeuroDiderot, INSERM1141, Université Paris Diderot, Sorbonne Paris Cité, F-75019 Paris, France
[5] Department of Computer Science, University of Warwick, Coventry, CV4 7AL, United Kingdom
[6] School of Life Science, University of Warwick, Coventry, CV4 7AL, United Kingdom
[7] Centre for the Developing Brain, Department of Division of Imaging Sciences and Biomedical Engineering, King's College London, King's Health Partners, St. Thomas' Hospital, London, SE1 7EH, United Kingdom.

[†]Equal contribution to the work
[‡] Equal contribution to the direction of the work
[§] Co-corresponding authors: s.ott@warwick.ac.uk; delara.saberan@univ-paris-diderot.fr; valerie.mezger@univ-paris-diderot.fr

[*] Present address: UMR CNRS 8638-Chimie Toxicologie Analytique et Cellulaire, Université Paris Descartes, Sorbonne Paris Cité, Faculté de Pharmacie de Paris, 4 Avenue de l'Observatoire, 75006 Paris, France

ORCID numbers : AL Schang, 0000-0003-1712-8505; J van Steenwinckel, 0000-0003-3463-4856; N Dyer 0000-0001-6158-0510; P Schäfer 0000-0002-0366-6858; B Fleiss, 0000-0001-7828-673X; D Sabéran-Djoneidi, 0000-0002-2757-6419; V Mezger, 0000-0003-1623-6213; P Gressens, 0000-0002-0909-4221;

BIOLOGICAL SCIENCES: Neuroscience; Systems Biology; Developmental Biology

FUNDING Information
VM was funded by CNRS, Université Paris Diderot, Agence Nationale de la Recherche (« HSF-EPISAME », SAMENTA ANR-13-SAMA-0008-01) and FRA 2015/16. DSD was funded by Paris Diderot University for travel grant for SO. ALS was supported by a postdoctoral fellowship by SAMENTA ANR-13-SAMA-0008-01. PG was funded by Inserm, Université Paris Diderot, ANR-13-SAMA-0008-01, Fondation Grace de Monaco, PremUP, Fondation des Gueules Cassées, ARSEP, and an additional grant from "Investissement d'Avenir -ANR-11-INBS-0011-" NeurATRIS. BF acknowledges support from Cerebral Palsy Alliance, Australia. PG and BF acknowledge financial support from the Department of Health *via* the National Institute for Health Research (NIHR) comprehensive Biomedical Research Centre award to Guy's & St Thomas' NHS Foundation Trust in partnership with King's College London and King's College Hospital NHS Foundation Trust. JL, CR, and KWA were funded by the Biotechnology and Biological Sciences Research Council (UK) through the Midlands Integrative Biology Training Partnership (MIBTP). The supporting bodies played no role in any aspect of study design, analysis, interpretation or decision to publish this data.

Author's contributions

ALS performed bioinformatics microarray and ATAC-seq dataset analyses, as well as wet experiments, including the MACS-isolation of O4+ OPCs and RT-qPCR experiments, in association with JvS (experimental design, mouse treatment and cell sorting) and TLC (cell culture, cytokine quantification by luminex). BF contributed to the design of the project, and brought very helpful suggestions along the experimental process and writing of manuscript.

SO, DSD, PG and VM codirected the work. SO supervised JL, CRG, KWA and ND in their input ATAC-seq analyses and developed bioinformatic tools for testing for enrichment of paired motifs of transcription binding sites, and also proposed and performed the bioinformatic comparison between the epigenomic landscapes of OPCs and inflamed HAECs. PS co-supervised JL and CRG. DSD played a major role in suggesting the use of ATAC-Seq, animated the collaboration with SO, and performed the MACs-isolation of OPCs and ATAC-Seq data experiments with ALS whom she co-supervised with VM and PG.

PG scientifically co-directed with VM the project. In particular, he was at the origin of the MACS-isolation of the OPCs and produced OPC transcriptomic datasets and initiated their analyses.

VM drove the study by proposing to analyze and intersect epigenomic data and transcriptomic data, for which she supervised DSD and co-supervised ALS; she wrote the paper with input from ALS, BF, SO, DSD, and PG.

Abstract

Premature birth is the commonest cause of death and disability in young children. Diffuse white matter injury (DWMI), provoked by inflammatory insults accompanying prematurity, is associated with increased risk of neurodevelopmental disorders – such as autism spectrum disorders – and is due to maturation arrest in oligodendrocyte precursors (OPCs). The lack of therapeutic solutions is a strong impetus to unveil the molecular mechanisms underlying neuroinflammation impact on OPC cell fate. We used a validated mouse model of DWMI, induced by systemic- and neuro-inflammation – as observed in preterm infants – and based on interleukin-1B administration from postnatal day P1 to P5. Using integrated genome-wide approaches we showed that neuroinflammation induced limited epigenomic disturbances in OPCs, but marked transcriptomic alterations of genes of the immune/inflammatory pathways. We found that these genes were expressed in control OPCs and physiologically downregulated between P3-P10, as part of the OPC normal developmental trajectory. We observed that transcription factors of the inflammatory pathways occupied DNA both in unstressed and inflamed OPCs. Thus, rather than altering genome-wide chromatin accessibility, neuroinflammation takes advantage of open chromatin regions and deeply counteracts the stage-dependent downregulation of these active transcriptional programs by the sustained upregulation of transcript levels. The intricate dual roles – stress-responsive and potentially developmental – of these proinflammatory mediators strongly suggest that the mere suppression of these inflammatory mediators, as currently proposed, may not be a valid neurotherapeutic strategy. Our study provides new insights for the future development of more targeted approaches to protect the preterm brain.

Keywords: neuroinflammation; epigenetics; transcriptomics; oligodendrocyte precursors; white matter injury; prematurity

Significance statement

Neuroinflammation provokes premature birth, the commonest cause of death and disability in children, including autism. Neuroinflammation-induced neurological damage encompasses white matter injury. The actual therapeutic strategies are orientated towards global repression of proinflammatory actors. We explore the epigenomic and transcriptomic impacts of neuroinflammation on a purified cell population of oligodendrocyte precursors cells (OPCs). Rather than altering genome-wide chromatin accessibility, neuroinflammation takes advantage of open chromatin regions and deeply counteracts the stage-dependent downregulation of these active transcriptional programs, in particular that of the inflammatory pathway. These proinflammatory genes are constitutively expressed by OPCs and their physiological downregulation during OPC maturation process is counteracted by neuroinflammation. The intricacy between the OPC physiological and neuroinflammation-responsive expression of these proinflammatory mediators reorientates neuroprotective strategies.

INTRODUCTION

Premature birth, namely birth before 37 of 40 completed weeks, occurs in 8-13 % of all births worldwide and is the commonest cause of death and disability in children under 5 years of age (1). Life-long morbidity is predominantly due to neurological damage, which altogether includes an array of effects, collectively called "encephalopathy of prematurity" (2). Almost 10% of infants born before 33 weeks develop Cerebral Palsy and approximately 35% have persistent cognitive and neuropsychiatric deficits, including autism spectrum disorders and attention deficit/hyperactivity disorder (3). Although the most severe problems stem from extreme prematurity, even slight reductions in gestational length have significant adverse effects. One of the hallmarks of encephalopathy of prematurity is diffuse white matter injury (DWMI), which is considered a key target for neuroprotection and the prevention of long-lasting handicap. DWMI is due to oligodendrocyte maturation arrest, leading to hypomyelination and ultimately to defects in grey matter connectivity (1, 4,5). In that context, neuroinflammation is a leading cause of encephalopathy of prematurity, serving as a central mediator of oligodendrocyte maturation defects and hypomyelination (6,7).

We have previously validated a mouse model of encephalopathy of prematurity that recapitulates arrest in oligodendrocyte maturation, hypomyelination, cognitive deficits and neuroinflammation, as seen clinically (8-11). In this model, the common exposure of preterm-born infants to systemic and central inflammation (neuroinflammation) that is known to drive encephalopathy is mimicked by intraperitoneal (i.p.) administration of interleukin 1B (IL1B) from postnatal days 1 to 5 (P1-P5). The similarities of this model to clinical conditions include that male mice are more severely affected than female mice (8,9). As such, the studies on OPC are performed in male animals. This developmental window (P1-P5) is equivalent to the high-risk window for encephalopathy of prematurity in infants, 23-32 week gestational age. This paradigm of preterm injury causes long-term myelination defects (8) suggesting that these prenatal adversities cause deviations from the delicately choreographed programs that control OPC maturation, creating a cell fate issue.

Here, using a purified population of premyelinating OPCs and integrated genome-wide approaches from this animal model, we have explored the contribution of epigenomic and transcriptomic disturbances to the OPC dysmaturation. We show that at P5 a limited number of chromatin regions are perturbed. We also find that the genes, whose expression levels are the most significantly altered by neuroinflammation, are involved in the immune system and inflammatory response. These genes, which include cytokines and chemokines, are unexpectedly expressed by OPCs, also in normal conditions, in a developmentally regulated manner: their expression is higher at early stages and downregulated at further steps of their maturation. The stage-dependent downregulation of these genes is perturbed in OPCs isolated from our inflammatory model of encephalopathy, which provokes a marked upregulation of their expression – likely participating to the failure of these cells to mature correctly.

These major transcriptomic disturbances surprisingly occur in genes which exhibit no overt changes in chromatin accessibility at P5. Indeed, our evidence suggests that neuroinflammation takes advantage of transcriptional programs that are active at the time of exposure – namely open chromatin regions - and disturbs their developmental regulation.

We have therefore unraveled a mechanism by which neuroinflammation acts on OPCs leading to maturation arrest in a model mimicking perinatal inflammation in preterm born infant. Indeed, the unexpected expression of numerous inflammatory genes by OPCs during their normal stage-dependent maturation likely paves the way for intricate interference between the response to neuroinflammatory insults and the white matter developmental program, with important implications for therapeutic strategies.

RESULTS

Characterization of O4+-purified cell populations used for exploration of the epigenome and transcriptome

In our previous studies we have demonstrated that oligodendrocyte maturation arrest is a hallmark of neuroinflammation triggered by IL1B intraperitoneal administration (IP). As outlined above and in Figure 1, IL1B was administrated (versus PBS as a control; Fig. 1; 8-11) between P1 and P5; this period mimics chronic exposure to systemic neuroinflammatory mediators from 23-32 weeks of gestation in the infant. Using magnetic-activated cell sorting (MACS), we isolated at P5 the premyelinating OPC population (O4+ OPCs) from male cortices in each

condition (Fig. 1). O4 is considered a pan-OPC marker in humans and mice (2, 8). We evaluated the purity of the O4+ population by performing RT-qPCR analyses, and demonstrated that this population, but not microglial (CD11B+) isolated fractions, expressed *Myelin binding protein* (*Mbp*) mRNAs (Fig. S1*A*). In addition, we found almost undetectable levels of the microglia marker mRNAs, CD11B (*Itgam*, *Integrin alpha M* gene) in the O4+ population. This suggests that this population indeed corresponds to premyelinating OPCs. Notably, we collected comparable numbers of O4+ OPCs from control (PBS) and treated (IL1B) samples (1.12 x 10^6+/- 0.12 x 10^6 cells per sample). In independent RT-qPCR experiments, as expected based on previous studies using this model (8), we observed that the expression of *Id2*, a transcriptional regulator associated with a pre-OPC maturation state, was increased in O4+ OPCs in response to neuroinflammation, whereas that of myelination-associated genes was reduced (Fig. S1*B*). Overall, these data show that the cell population isolated by our MACS-protocol is predominantly enriched with O4+ OPCs and that this isolated O4+ OPC population exhibits hallmarks of maturation arrest, as expected in response to neuroinflammation induced by intraperitoneal administration of IL1B.

The epigenome of OPCs is globally preserved in response to systemic IL1B exposure

We first investigated the impact of IL1B on the integrity of the chromatin landscape in OPCs using ATAC-Seq (12; *Assay for Transposase-Accessible Chromatin with high-throughput sequencing*; Fig. 1). This approach harnesses the ability of the Tn5 transposase to integrate a DNA fragment into open chromatin regions, allowing to sensitively and accurately map accessible regions. Using the bioinformatics workflow described in Fig. S1*C* (see Material and Methods) including the MACS2 and EdgeR software tools, we obtained an average of 72 million Tn5-integrated mapped reads per sample, representing a total of 213,246 statistically significant peaks (MACS2; FDR < 0.05; Table S1 and S2; Dataset S1). Analysis of the insert size distributions showed the expected nucleosome-induced pattern and the 10.4bp periodicity with good consistency across samples, an indication of high data quality (Fig. S1*D*).

The number of reads, which reflects chromatin accessibility, was determined for each sample in the 213,246 peaks. We performed principal component analysis (PCA) on our samples and observed that principal component 1 (PC1) accounted for 42% of the variance and separated samples from control and neuroinflammation-exposed OPCs (Fig. 2*A*). This shows that a large proportion of the variance in this dataset can be explained by the IL1B exposure. We obtained similar results using the EdgeR MDS function (Fig. S2*A*). Among the 213,246 significant peaks, only 524 peaks were open or closed in response to IL1B (FDR < 0.05, Fig. 2*B*; Fig. S2*B*; Table S3). The majority of peaks with differential chromatin accessibility was more open in IL1B, compared to PBS conditions (Fig. 2*B,* Fig. 2*C*). The extent of changes to chromatin accessibility was small, with fold-changes of most peaks only mildly deviating from sample-to-sample variability (Fig. 2*B*). The median fold-change of differentially open regions was only 2-fold (2.03).

We next annotated the 213,246 peaks using HOMER annotatePeaks function. Peaks were mostly distributed in intergenic and intronic regions and were enriched in gene regulatory regions and gene bodies (Fig. S2*C*). A similar distribution was observed for the 524 differential peaks (Fig. S2*C*). Representative peaks showing increased, reduced, or unchanged chromatin accessibility are illustrated in Fig. 2*D* and Fig. S2*D*. We assigned differential peaks to genes based on proximity to their transcription start site (TSS) and thus likely affected by chromatin alteration, and performed gene ontology (GO) analyses, using David6.8, for the 485 corresponding genes, of which 344 were assigned a GO-term. The top ten GO-terms ranked according to their FDR, belong to pathways relevant for neural development (regulation of cell migration, cell adhesion, and neuron projection development, but none of them showed FDR < 0.05; Fig. S2*E*; Table S4).

Our results thus reveal that only 0.25% of open chromatin regions show differential chromatin accessibility in P5 OPCs that are isolated from a model of inflammation-driven encephalopathy.

Impact of systemic IL1B exposure on the transcriptome of O4+ OPCs

We analyzed gene expression in isolated O4+ OPCs using microarray analysis. We compared six independent samples of O4+ OPCs from IL1B-exposed mice to six independent samples from PBS (control) mice. IL1B-exposure mainly induced upregulation of gene expression: 1,266 genes were up-regulated and 454 downregulated, which corresponded to 1,872 and 699 probes, respectively (FC +/-1.5; FDR < 0.05; Fig. 3*A*; Table S5). As expected based on previous work in this model (8) and from our validation experiments by RT-qPCR for O4+ OPC isolation (Fig.

S1*B*), the analysis of our microarray data revealed that the expression of genes associated with myelination (*Mbp*, *Mog*, *Mag*, *CNPase*, *Plp1*; which are still lowly expressed at P5 in normal conditions) were downregulated by IL1B, whereas that of *Id2* was upregulated (8; Fig. S3*A*). These results indicated that our samples and microarray analyses were representative of OPC maturation blockade (8). The GO analysis of these upregulated genes strikingly pinpointed the immune system and inflammatory response in the top 5 most statistically significant pathways (DAVID 6.8; Fig. 3*B*; Table S6). The analysis of downregulated genes indicated that these belonged to pathways linked to development, but with lower statistical relevance (Fig. S3*B*). Our microarray data highlighted that the significant alteration in the expression of the 262 genes, belonging to the immune system and inflammatory response pathways, mostly corresponded to upregulation (Fig. 3*C*). Using RT-qPCR on independent samples, we confirmed the induction of the expression of known players of these pathways: cytokines, chemokines, interleukins and their receptors (Fig. 3*D*).

OPCs intrinsically activate genes of the immune and inflammatory pathways in response to IL1B

We excluded the possibility that the upregulation of immune and inflammatory genes was due to contamination of O4+ OPCs with microglia. In this model of neuroinflammation we have previously published microarray analyses of the transcriptomic profiles in microglia (CD11B+ MACS-isolated cells; 9). These CD11B+ cells were obtained from the same animals as the O4+ OPC populations that we have examined in this study; by sequentially MACS-based isolation of O4+ OPCs and CD11+ microglia cells from the same brains. We compared the microarray gene expression profiles in the previously assessed CD11B+ cells to the list of 262 genes found in OPCs and corresponding to inflammation and immune pathways (Fig. 4*A*; Fig. S4; dataset from 9). These two cell populations exhibited remarkable differences in gene expression profiles in response to neuroinflammation, both in the magnitude and direction of expression changes; Fig. 4*A*; Fig. S4). Notably, the upregulation of these genes in microglia was greatest at P1 and their expression at P5 has already recovered, reaching basal levels comparable to that of PBS samples, while in OPCs the basal expression has not (9; Fig. 4*B*). Those data were confirmed by RT-qPCR in independent O4+ OPC and CD11+ samples, and extended to astrocytes (GLAST+ MACS isolation). Specifically, neither CD11B+ microglia, nor GLAST+ astrocytes showed an increase in the expression of selected cytokines and chemokines at P5 (illustrated here for *Ccl2*, *Cxcl1* and *Cxcl10*; Fig. 4*B*). Altogether, these results indicate that the upregulation of immune and inflammatory pathway in O4+ OPCs in response to IL1B in our microarray analyses at P5 cannot be attributed to contamination of OPCs by microglia, nor astrocytes.

To verify the potential for production of inflammatory players by OPCs in response to inflammation, we isolated primary OPCs, grew them *in vitro* and treated these cultures with IL1B (Fig. 5*A*). We detected significant induction of the production of seven cytokine and chemokine proteins *via* Luminex in the supernatant of IL1B-treated MACS-isolated primary O4+ OPCs, cultured for 24 or 72 hours (Fig. 5*B*). We also confirmed the upregulation of these inflammatory and immune mediators at mRNA levels (Fig. S5*A*).

In conclusion, these data strongly support the hypothesis that, at P5, O4+ OPCs are able to intrinsically synthesize inflammatory and immune pathway proteins in response to exposure to inflammatory stimuli.

Linking chromatin and transcriptional disturbances in response to IL1B exposure

To examine the contribution of modifications of chromatin accessibility to the changes in the transcriptome, we intersected our ATAC-Seq data (213,246 peaks, corresponding to 20,108 gene names) and our microarray data (limited to genes with annotated ID; 25,294). We found 16,883 genes in common between the two datasets, of which 1,333 genes showed altered expression after IL1B exposure and 404 peaks showed differential chromatin accessibility. By performing the intersection of the 1,333 differential genes with genes nearby the differential 404 ATAC-Seq peaks, we identified 53 genes representing a statistically significant overlap between transcriptomic and epigenomic changes. (Fig. 6*A*; $p= 1.7\ e^{-4}$; Table S7).

In order to maximize the chance of attributing peaks to relevant genes, we reasoned that peaks corresponding to opening or closing of the chromatin and lying within +/- 8kb around a TSS were most likely to contribute to the regulation of the expression of the corresponding gene. Taking this into account, we identified 15 genes showing differential expression and exhibiting modifications of the chromatin landscape in their vicinity, which

corresponded to 20 % of the ATAC-Seq peaks present in +/- 8 kb around the TSS (Fig. 6*B*; p= 8.74 e^{-5}; Table S8). Among these 15 genes, 10 corresponded to genes involved in the immune system and inflammatory response pathways: *Cd14, Cwc22 (*Fig. 2*D), Hmha1, Ifit3, March1, Nckap1l, Slfn2, Slc15a3, Tlr1, Tnfsf14, Tnfrsf12a* (Table S8). Interestingly, *Hif3a*, a gene recently identified in models of inflammation, was also included in this list (see discussion; Fig. 2*D*).

In summary, the immune system and inflammatory response pathways were prominently represented in the lists of genes showing marked dysregulation of their expression upon IL1B treatment, and associated to two different chromatin behaviors: 1) a limited number of genes shows differential chromatin accessibility upon IL1B exposure (Fig. 6*A* and *B*); 2) the majority of the genes annotated in the top 5 most enriched GO-terms displays no major changes in chromatin accessibility (Fig. *3B*). Indeed, in this case, the chromatin was already in an open conformation in the PBS samples (examples shown in Fig. S2*D*).

Identification of combinatorial transcription factor binding in immune system and inflammatory pathways

In the large majority of instances where neuroinflammation altered gene expression, we observed that the chromatin was already open and remained unchanged. As such, we investigated the putative involvement of transcriptional regulators as primary mediators of alteration in gene expression. We searched for enrichment in transcription factor (TF) binding sites (TFBS) using HOMER and known motifs in the ATAC-Seq peaks adjacent to differentially regulated genes (up and downregulated genes, termed “ALL”). We chose to focus on ATAC-Seq peaks within a distance of +/- 8 kb relative to the TSS of these genes. Members of the IRF (interferon-regulatory factor) family appeared at the top of the list with the strongest scoring results. This is also true for the composite site PU.1-IRF8, and NFκB family members (Fig. S5*B*). A list of similar motifs was found with comparable scoring results, as well as p-values, in the peaks adjacent to upregulated genes (termed “UP”; Fig. S5*C*).

Because we suspected that these TFs might work together (13), we investigated the occurrence of paired motifs in the peaks located in +/- 8kb regions around the TSS of differentially regulated genes, as described in Materials and Methods. The analysis of peaks corresponding to downregulated genes did not reveal any paired motif enrichment, compared to random occurrence in all peaks. In contrast, the analyses of ATAC-Seq peaks associated with upregulated genes revealed the existence of paired TFBS motifs, with marked involvement of TFBS from the IRF family, PU.1/SPI1, *Isre* (Interferon-Stimulated Response Element), NFκB, and AP-1 family (Fig. 6*C*; Table S9).

To investigate whether the occurrence of these motifs corresponded to the binding of TFs, we tested the motif occupancy on DNA in PBS and IL1B conditions. For this, we used the Wellington algorithm (14), which is highly accurate in inferring protein (TF)-DNA interactions. We investigated the presence of footprints corresponding to occupied TFBS and their motif content, located within significant ATAC-Seq peaks, adjacent to differentially regulated genes. The average footprint profiles, produced for the top 6 results in the list of known HOMER motifs (Fig S5*B,C*) are illustrated, for IRF1, IRF2, IRSE and NFκB in Fig. 6*D* (using data from both conditions, PBS plus IL1B) and in Fig. S6*A* (PBS, upper panels; IL1B, lower panels). The dip in the number of reads at the center of the sharp average profile (indicated by brackets) was strongly suggestive of effective TF binding. A similar analysis is illustrated for IRF1, IRF2, IRSE, and NFκB (Fig. S6*A*). In contrast, PU.1-IRF8 and PGR (Progesterone Receptor) average footprint exhibited sharp internal spikes, suggestive of transposase insertion bias (15, Fig. S6*B*). Interestingly, there was little difference in the average footprint profiles for all these TFs, when considering either PBS samples only or IL1B samples only, indicating that these TFs might already bind DNA at the corresponding motifs in PBS conditions (*Fig. S6A*).

Altogether, these results indicate that key TFs involved in the immunity and inflammatory processes are bound in a significant number of open regions located in the vicinity of genes that are differentially upregulated by IL1B. The binding of such TFs is coherent with the prominent upregulation of proinflammatory cytokine and chemokine genes, and other genes of the immune system and inflammatory pathways. In addition, because footprint profiles were similar in PBS and IL1B conditions, our data suggest that, at P5, these TFs might be positioned in these regions before exposure to IL1B.

There was no evidence for footprints in peaks adjacent to downregulated genes (data not shown). And the search

for de *novo* motifs in ATAC-Seq peaks near differentially expressed genes did not reveal statistically relevant motif associated with *bona fide* average footprints (data not shown).

Constitutive expression of genes of the immune and inflammatory pathways at early stages of OPC maturation trajectory, in unstressed conditions

At this step of the study, we had shown that P5 isolated O4+ OPCs were able to induce the expression of genes belonging to the immune system and inflammatory response pathways, in response to neuroinflammatory challenge. We had also shown that these major alterations in gene expression occurred without major modifications in chromatin accessibility, but that key TFs controlling these pathways were bound to these open regions both in the control (PBS) and neuroinflammatory (IL1B) conditions. These observations suggest that the epigenomic profiles associated with IL1B-induced genes exhibit neuroinflammatory-like patterns prior to IL1B exposure (*i.e.* open chromatin conformation). Furthermore, transcription of these genes may already be activated at a physiological level in OPCs during normal development and further upregulated by exposure to neuroinflammation.

To assess this hypothesis of the transcription of immune and inflammatory genes in normal OPC maturation trajectory, we MACS-isolated O4+ OPCs at P3, P5, and P10 from our model of preterm neuroinflammatory injury. Indeed, our investigations detected presence of cytokine and chemokine mRNA in O4+ OPCs in control conditions. These mRNA levels were greatest at P3 and decreased in a stage-dependent and significant manner, between P3 and P10 (Fig. 7*A* and Fig. S7*A*). In addition, we verified that our control condition (i.p. PBS) did not constitute a stress, *per se*, that would induce the expression of cytokine and chemokine genes in the absence of IL1B administration. By comparing MACS-isolated O4+ OPCs from naïve (untreated) and PBS-treated pups at P5 we observed similar levels of cytokine and chemokine gene expression, in RT-qPCR experiments (Fig. S7*B*). This shows that PBS injection is not responsible for constitutive cytokine and chemokine mRNA levels at P5. In contrast, IL1B-treated OPCs exhibited elevated levels of cytokine and chemokine mRNAs compared to naïve or PBS OPC samples, as expected (Fig. S7*B*). Moreover, we confirmed that the constitutive expression of cytokines and chemokines also occurred in normal conditions in the murine oligodendrial cell line, Oli-neu (Fig. 7*B*). We showed that this constitutive expression decreased during Oli-neu differentiation, as was observed during the O4+ OPCs maturation trajectory (Fig. 7*B* and Fig. S7*C*). These data demonstrated that O4+ OPCs can intrinsically transcribe cytokine and chemokine genes at an early OPC stage (P3), and that the expression of these genes is gradually downregulated during their maturation process between P3 and P10, in a physiological and developmental manner. This constitutive transcription is in line with the small scale and extent of the open chromatin changes of these genes that we observe at P5 (Fig. S2*D*).

To further confirm our findings, we formulated and performed an additional analysis, taking advantage of an existing public ATAC-seq dataset from a similar control versus treatment study, which used IL1B stimulus on human adult aortic endothelial cells (HAECs) isolated from aortic trimmings of donor hearts (16; "HAEC dataset"; NCBI Gene Expression Omnibus; accession no: GSE89970). Through a cross-species comparison, our aim was to explore global chromatin landscape similarities (or lack thereof) between both control and IL1B-treated, HAEC and O4+ OPC, samples. First, both datasets were limited to chromatin regions annotated with matching 1-to-1 gene orthologs and located within ±2 kb of a TSS as described in Material and Methods. In total we were able to match 7,739 peaks, between the two datasets, including 100 regions, which were found to be differential between the control and IL1B conditions, in the HAEC dataset. Subsequent cross-comparison of these regions reported no significant difference between both O4+ OPC samples and the HAEC IL1B-treated sample. In contrast, both O4+ OPC samples showed significant differences (p-value < 10^{-15}) to the HAEC control sample (Fig. 7*C*; Fig. S7*D*; Table S10). These findings reveal a characteristic IL1B pattern in the chromatin profiles of OPCs isolated from both inflammation-exposed and control mice, which is indicative of an inflammation-like signature that is already present at basal level in developing OPCs. The results thereby reinforce our findings about cytokine and chemokine gene expression in unstressed and stressed O4+ OPCs.

DISCUSSION

Overall, our results indicate that the remarkable capacities of premyelinating O4+ OPCs to produce immunomodulators constitute one route of entry for the impact of neuroinflammation on OPC maturation. Indeed, the developmental control of their synthesis is highjacked by neuroinflammation and this process occurs with limited effects on chromatin accessibility. Rather, we observe that neuroinflammation mainly takes advantage of the presence of open chromatin regions corresponding to active transcriptional programs, of which the constitutive expression of genes of the immune and inflammatory pathways, in normal conditions, is the most prominent target for neuroinflammation-induced disturbances.

The impact of neuroinflammation can thus be interpreted in the following way: by markedly increasing the levels of cytokine and chemokine gene expression at P3 and P5, neuroinflammation produces a delay in the normal downregulation of these genes at P5, and, therefore, maintains abnormally elevated levels of these players at this stage. This suggests that one major mechanism for neuroinflammation-induced OPC maturation blockade operates by interfering with the normal stage-dependent expression and downregulation of players of the inflammation pathway, along the OPC maturation trajectory.

Our data also nurture an underlying and emerging concept: molecules that have been historically identified and studied as key mediators of stress responses and guardians of cell or organism homeostasis are also pivotal in physiological conditions for normal development. Emblematic examples are represented by TF families, like NFkB (17) and HSF (Heat Shock Factors) and their target genes encoding the heat shock proteins (HSPs; 18; 19; 20). Whether these two apparently distinct functions might have emerged concomitantly in evolution or not is unclear, but for technical and practical reasons, the roles of these molecules in normal development have been understudied. The production of inflammatory players by prenatal OPCs and its role in brain formation is therefore less unexpected than it appears.

Accordingly, it has been extensively reported in the literature that OPCs and mature oligodendrocytes of the adult brain can express key players of immune and inflammatory pathways in pathological conditions. This includes studies of patients affected by multiple sclerosis (MS) or in *in vivo* models of experimental autoimmune encephalomyelitis (EAE; reviewed in 21). Here, we show that P5 O4+ OPCs express genes and proteins associated with inflammatory pathways in normal conditions. As such, OPCs during normal development thus display properties similar to that ascribed to adult OPCs and mature oligodendrocytes, which can shape the inflammatory environment, or in the perspective brought by the new concept mentioned above, that they perform a trophic role on their environment at defined time-windows. Our results are also in line with previous results showing that OPCs, derived *in vitro* from neurospheres, can activate cytokine genes in an EAE model (23). In a more original manner, we also unravel the physiological, constitutive expression of cytokine and chemokine genes in normal O4+OPCs at an early postnatal stage. In line with our findings, Zeis et al. (21), revisited published microarray data sets (23) and pointed out the expression of genes belonging to the GO:term “immune system process”, in PDGFRa+ unstressed OPCs, which reinforces our data.

Only a limited number of genes belonging to the immune system and inflammatory pathways, and whose expression is dysregulated by exposure to neuroinflammation undergo significant chromatin remodeling. Hypoxia-Inducible Factor 3, *Hif3a*, is one of them and was shown to be regulated, in an oxygen-independent manner, in two distinct models of inflammation, in non-neural cells (24,25). Interestingly, in parallel of our data, Cuomo et al. (25) established that proinflammatory cytokines are responsible for the activation of the *Hif3a* gene, through epigenetic changes and the involvement of NFκB. Nevertheless, another possibility is that the bulk of genes of the immune and inflammatory pathways, which show no major alteration in chromatin confirmation, could exhibit minor, but crucial differences in nucleosomal positioning that would correlate with major increase in transcription (positioning of the first nucleosome and phasing of the following ones). Such subtle modifications, but no major changes in chromatin accessibility, have been strikingly identified during ES cell differentiation along diverse cell lineages (for example, 26). Future studies will determine whether the restricted impact of neuroinflammation on chromatin accessibility in the premyelinating OPC reflects an intrinsic robustness of the epigenome. Alternatively, the epigenome might have been perturbed at earlier stages and have already recovered at P5. In both cases, the molecular bases underlying this robustness or recovery capacities remain to be explored.

Another question is the functional impact of the opening or closing of the chromatin in response to neuroinflammation, in regions that we have identified by ATAC-Seq. As already mentioned, most of them do not correlate with major transcriptional changes. This raises three interpretations. Firstly, the transcriptomic impacts of these epigenomic modifications might be "buffered"/minimized, thanks to the binding of different sets of TFs, which would deserve further investigations. Secondly, TFs, which are multifaceted drivers, remodel the chromatin state and genome topology, often before changes in gene expression can be observed, as was demonstrated in studies on the molecular basis of cell fate (27). These modifications of the chromatin landscape could thus constitute an Achilles' heel for transcriptomic disturbances, that would occur either at later maturation stages, at temporal distance from the insult, or upon a second hit of neuroinflammation. The occurrence of additional inflammatory insults is relevant because, besides exposure to prenatal inflammatory insults - which is mimicked by our model -, preterm babies also face a heavy burden in terms of postnatal inflammatory insults, representing additional neuroinflammatory hits (28). Thirdly, one other exciting possibility is that, in the genome, these TFs involved in immune and inflammatory pathways might also work at long-distance from their dysregulated target genes, which would involve remodeling at multiple architectural levels (chromatin looping, TADs (tolopogically associated domains) connectivity etc.).

Besides these considerations, the entry route for neuroinflammation is represented by the constitutive and stage-dependent synthesis of cytokines and chemokines by premyelinating OPCs in normal conditions, which empowers neuroinflammation to impact OPC maturation. This entry route can thus be envisioned as recapitulating and intermingling both injurious and developmental aspects, as already expected from the field (29). Indeed, by counteracting the tightly regulated physiological expression of cytokines and chemokines by O4+ OPCs at P3, that is programmed to gradually decrease in a developmental, stage-dependent manner (here shown between P3 and P10), the neuroinflammatory insult might compromise the premyelinating OPC cell fate. In line with our results, Moyon et al. (30) pointed out the role of IL1B and CCL2 production by premyelinating OPCs in modulating their motility capacities and eventually differentiation (see also 25). In addition, this production could regulate the recruitment by OPCs of other cells (like microglia; 32,33) that are known to influence OPC maturation. Notably, as it is the case for other pathways historically identified as stress-responsive, like the HSF pathway, which is also involved in unstressed conditions during physiological brain development, the order of magnitude of the up- or downregulation of target gene expression (here chemokines and cytokines) is lower during development than it is in response to stress exposure (Fig. 7*A*).

In conclusion, in the context of a chronic–perinatal systemic inflammation, the epigenome seems globally preserved in premyelinating OPCs, in terms of chromatin accessibility, and the contribution to OPC blockade is mostly driven by transcriptomic disturbances. These transcriptomic perturbations concern transcriptional programs that are already open at the time of exposure, and most prominently the immune system and inflammatory pathways. Our results have important therapeutic consequences: because of the striking intertwining between the injurious and developmental facets of these inflammatory mediators, we should reconsider that global targeting of this pathway might constitute a therapeutic option. One conclusion emerging from our study is that the TFs involved in response to neuroinflammation in OPCs seem to be already at play in normal OPCs to control the developmental transcription of these genes. In addition, they work in combination as suggested by their pairing profiles. Our work thus paves the way of future studies that would allow the design of a therapeutic strategy, based on subtle manipulation of the activity of TFs, using appropriate cocktails of low-dose modulators.

MATERIALS AND METHODS

Animal Model

Experimental protocols were approved by the institutional review committee and met the guidelines for the United States Public Health Service's Policy on Humane Care and Use of Laboratory Animals (NIH, Bethesda, MD, USA). Sex was determined at birth, and confirmed by abdominal examination at sacrifice. This animal model is similar to the human in that males are more affected and, as such, only male OF1 pups were used, as female OPCs maturation is not altered (8). IL1B injections were performed as described (8,9). Five µL volume of phosphate-buffered saline (PBS) containing 10µG/kG/injection of recombinant mouse IL1B (R&D Systems, Minneapolis, MN) or of PBS alone (control) was injected intraperitoneally (i.p.) twice a day on days P1 to P4 and once a day on day P5 (see Fig. 1). Pups were sacrificed four hours after the morning injection of IL1B at P3 or P5, and at a similar time at P9, or P10. ATAC-Seq data were produced from 3 independent biological replicates for each condition (PBS or IL1B; Fig. 1). Microarray data were produced from 6 independent biological replicates for each condition (PBS or IL1B; Fig. 1), using the same animals that were also analysed for CD11B+ microarrays (9).

O4+ magnetic and microglial activated cell sorting in mouse

O4+ cells were isolated at P3, P5, P9, or P10 by Magnetic Activated Cell Sorting (MACS, Miltenyi Biotec, Bergisch Gladbach, Germany), according to the manufacturer's protocol and as previously described (34). Briefly, brains were collected without cerebellum and olfactory bulbs, pooled (3 brains per sample) and dissociated using the Neural Tissue Dissociation Kit containing papain. O4 + cells were then enriched by MACS, using the anti-O4 MicroBeads. For microarray and RT-qPCR analysis, the eluted isolated cells were centrifuged for 5 min at 600g and conserved at -80°C. CD11+ microglial cells were isolated as described (9). The unlabeled fraction mainly contained astrocytes (see Fig. S1*A*). For the ATAC-seq experiment, 50,000 cells were immediately lysed and their nuclei submitted to Tn5 activity. The purity of the eluted O4-positive fraction was verified using qRT-PCR for Myelin Basic Protein (*Mbp*), ionizing calcium binding adapter protein (*Iba1*), glial fibrillary acid protein (*Gfap*) and neuronal nuclear antigen mRNAs (*NeuN*; Fig. S1*A*).

OPC culture and differentiation

OPCs were prepared from newborn OF1 mice as described (35,36). In brief, forebrain cortices were removed from postnatal day 0–2 mouse pups and freed from meninges. Minced tissues were enzymatically digested with 0.125% trypsin (Sigma) and 0,0025% DNase I (Sigma) for 15 min at 37°C and then mechanically dissociated. Cells were filtered through a 100-µm-pore-size cell strainer (BD), centrifuged 10 min at 1800 rpm, resuspended in minimum essential Eagle's medium (Sigma) supplemented with 10% FBS (Gibco), 1% Glutamax (Gibco), 1% penicillin-streptomycin (P/S) solution (Sigma), and 0.5% glucose and plated in T75 flasks at a density of $2 \times 10^5/cm^2$. Mixed glial cell cultures were grown until confluence for 9-11 days (medium was replaced every 48-72h) and shaken for 1.5 h at 260 rpm to detach microglia. These detached microglia were then collected and removed together with the media. Remaining cells were shaken for additional 18h to detach the OPCs from the astrocyte base layer, and were simultaneously treated with 100 µg/ml liposomal clodrosome suspension (Clodrosome®, Encapsula Nanosciences, Brentwood, USA) which selectively eliminates any residual microglia. The detached OPC cell suspension was filtered through a 20-µM-pore-size filter (Millipore) and incubated in an untreated Petri dish for 10 min at 37°C to allow attachment of any remaining microglia. Purified OPCs were then seeded onto poly-D-lysine-coated 12-multiwell plates at a density of $3 \times 10^4/cm^2$ in OPC proliferation medium composed of Neurobasal medium (Gibco), 2% B21 (Miltenyi biotec), 1% P/S (Sigma) and 1% Glutamax (Gibco), supplemented with growth factors consisting in 10nG/mL FGFα (Sigma) and 10nG/mL PDGFα (Sigma). After 72h, OPC differentiation was initiated by growth factor withdrawal and addition of 40 nG/mL of T3 (Sigma). At the same time, OPCs were treated with 50nG/mL IL1B (R&D Systems, Minneapolis, MN) or PBS for 4h, treatment was removed, new media provided and cells were grown in differentiation medium until 72h (Fig. 5*A*).

Oli-neu cell line culture and differentiation

The immortalized murine OPC cell line, Oli-neu, was kindly provided by Dr Sheila Harroch (Pasteur Institute, Paris, France). Oli-neu was established from OPC-enriched murine primary cultures from E16 brains transformed with a provirus containing the oncogene *T-Neu* (37). Various differentiation protocols have been established, among which treatment with PD174265, a selective inhibitor of the activity of Epidermal Growth Factor receptor (ErbB) tyrosine kinase, has been shown to induce MBP expression (38). These cells were cultured in Dulbecco's modified Eagle's minimum essential medium (DMEM) containing Glutamax 1X and high glucose (4.5 G/L) (Gibco 31966), supplemented with 1 mG/mL insulin (Sigma), N2 supplement (Gibco), 100 µG/mL T4 and T3 (Sigma), 1% horse serum (Gibco), and 1% P/S (Sigma). At confluence, the cells were mechanically detached and seeded in 12-multiwell plates at a density of 15,000 cells/cm². After 24h, differentiation was induced by addition of 1µM PD174265 (ChemCruz) diluted in DMSO at 1 mM. Medium was replaced after 48h and differentiation was stopped after 72h. Another differentiation protocol using one third of conditioned medium from primary neuronal culture was also used (39; Fig. S7*C*).

RT-qPCR analysis and Luminex assay

Preparation of samples for quantitative reverse-transcriptase polymerase-chain reaction (qRT-PCR), primer design PCR protocol and luminex assay were similar to that previously described (39). Primer sequences are given in Table S11. *Gapdh* (glyceraldehyde-3-phosphate dehydrogenase gene) and *Rpl13* (Ribosomal Protein L13) were chosen to standardize the quantitative experiments based on reference gene suitability testing.

ATAC-Seq analysis in O4+ OPCs

ATAC-seq protocol was performed as described (12) with slight modifications. In brief, cells were immediately lysed after cell sorting and a total of 50,000 nuclei were subjected to Tn5-mediated transposition for 30 min, resulting in 'tagmented' DNA fragments. Tagmented DNA was purified on MinElute colums (Qiagen) and amplified/tagged in two steps using NEBnext High-Fidelity 2x PCR master mix (New England Biolabs). Amplified DNA was purified twice with 1.8 volumes of NucleoMag NGS Clean-up and Size Select beads (Macherey Nagel). DNA was quantified using the Qubit dsDNA HS Assay Kit and the quality of each library determined on Agilent 2100 Bioanalyzer DNA High Sensitivity ChIPs. Libraries demonstrating appropriate nucleosomal profiles were multiplexed and subjected to Illumina NextSeq500 sequencing (IGenSeq Platform, ICM, Paris, France). Fastq files are available in Dataset S1. The main steps of sequence analyses are summarized in Fig. S1*C*. After quality controls (Fastqc and Trimmomatic 0.33), reads were aligned on the mm10 genome with Bowtie 2 (Galaxy tool version 2.3.4.1 (41; default parameters) (Table S1; Fig. S1*C*). Peak calling was performed with MACS2.2.0; default parameters; q<0.05) separately for the two conditions, using a pooled (n=3) bam file of control samples and a pooled (n=3) bam file of IL1B samples. The two resulting bed files were merged and, after removing the mm10 blacklist (http://mitra.stanford.edu/kundaje/akundaje/release/blacklists/mm10-mouse/mm10.blacklist.bed.gz), 213,246 DNA regions (peaks) significantly detected in at least one condition were delimitated (Table S2). The number of reads was determined in each peak for each sample using Bedtools coverage (version 2.19.1) and normalized to the library sizes. Principal component analysis was performed on log transformed read count values of the top 500 most variable peaks, using the prcomp function in R. Differential peak detection between the three PBS and the three IL1B samples was performed with the Bioconductor software package EdgeR (3.22.3; 40) using R studio (0.98.1103; http://www.rstudio.com). Statistical comparison was performed using the exact test function followed by False Discovery Rate (FDR) determination by the Benjamini-Hochberg method.

Linking of HAEC and OPC ATAC-Seq datasets

We used a public ATAC-Seq dataset of human aortic endothelial cells (HAECs; 16; NCBI Gene Expression Omnibus; accession no: GSE89970) and processed the raw reads (using the hg19 reference genome) to obtain a set of peaks. Both sets of peaks (control and IL1B-treated samples) were annotated using HOMER's annotatePeaks function. Next, HAEC peaks were matched to mouse OPC peaks through gene annotations, by taking only those peaks annotated with matching orthologous genes (only 1-to-1 orthology was considered). Matching was further restricted to

promoter regions (peaks with a relative maximum distance of 2kb from the TSS). In order to ensure that peaks were true matches, this set was further restricted to a relative distance of 500 bp from each other in relation to the TSS. Using this approach, a total of 7,739 peaks were matched between the HAEC and OPC datasets, including 100 peaks identified as differential in the HAEC dataset using DESeq2. Next, the number of reads mapped to matched peaks were obtained by counting the number of reads at the summit ± 50bp using the featureCounts package of the Subread software (v1.6.0) and the counts were normalized against the total number of reads present in all matched peaks and converted into reads per million. Normalized read number distributions of the two datasets were compared using the one-sample Wilcoxon rank test with continuity correction.

Microarrays of mouse O4+ OPC gene expression and data preprocessing

Microarray analysis was performed on six control and six IL1B samples (O4+ cells isolated at P5 after *in vivo* PBS or IL1B treatment) using Agilent Whole Mouse Genome Oligo Microarrays 8x60K (Agilent). Raw data are available in Dataset S2. All the steps, from RNA extraction to statistical analysis, were performed by Miltenyi Biotec, as previously described (34). In brief, intensity data were subjected to quantile normalization, unpaired t-tests (equal variance) were conducted to compare intensities between the two groups for each probe and p-values were adjusted through FDR determination by the Benjamini-Hochberg method. Fold changes correspond to the median ratios (median[IL1B]/median[PBS]). When FC<1, the FC was expressed as a negative value using the formula FC(neg)=-1/FC. For example, if FC=0.5, the indicated FC is -2. Probes with FDR <0.05 were considered significant. An additional fold change (FC) threshold was chosen at +/- 1.5 (corresponding to FC>1.5 and <0.666).

Heat map representation

Heat maps were created using Morpheus (https://software.broadinstitute.org/morpheus). The Log2 median-centered data were visualized using a fixed (nonrelative) color pattern. The color scales are indicated on each heatmap. Rows and columns were submitted to hierarchical clustering with the following criteria: metric = one minus Pearson correlation, linkage method = average.

GO-term enrichment analysis

GO-term Biological Pathway enrichment was done using David 6.8 (42,43).

TFBS motif enrichment analysis, and TF footprint analysis

The 213,246 significant peaks detected by MACS2 in at least one condition (PBS or IL1B) were annotated with the *HOMER annotatePeaks* function. The list was restricted to the peaks located between -8000 and +8000 bp from the closest TSS ("TSS-All" list). Among this list, peaks were selected, which were annotated with a gene name and for which the gene expression was modulated in the microarray analysis (FDR<0.05 and FC>1.5 or <-1.5). The full list of peaks and lists restricted to up or down-regulated genes were submitted to motif enrichment analysis using *HOMER FindMotifsGenome* with the options "-size given" and "-mask". The "TSS-All" list was used as background. Six motifs corresponding to the top 5 motifs enriched in the full list of peaks (ISRE, IRF1, IRF2, Nfkb-p65 and PGR, Figure S5B) and the 15th motif enriched in the list restricted to up-regulated genes (PU1:IRF8, Figure S5B) were localized in the full list of peaks (UP+DOWN) with *HOMER FindMotifs*. For each of these motifs, the average profile of Tn5 activity was visualized using *pyDNAse* dnase_average_profile.py (14). This profiling was performed using a pooled bam file of PBS samples, or a pooled bam file of IL1B samples separately, and a pooled bam file of the two conditions ("both") together.

Testing for enrichment of paired motifs

2319 ATAC-Seq peaks corresponding to 1266 upregulated genes (886 different gene names) and 946 ATAC-seq peaks corresponding to 454 downregulated (336 different gene names) were tested for significantly enriched pairs of TFBS relative to a universe containing all the peaks located +/- 8 kb around the closest TSS. For each individual motif from the homer database, all peaks in the universe were ranked by motif occupancy using a binomial score. Then for every possible pair of motifs, peaks containing both motifs were identified using the overlap between top 5000

ranked peaks for each of the individual motifs. A hypergeometric test was used to calculate the enrichment score (p-value) for the overlap between each test set and the peaks containing both motifs. The resulting p-values were corrected using the Benjamini-Hochberg correction.

Statistical analysis

All *in vivo* and *in vitro* experiments were performed using an alternating treatment allocation. All analyses were performed by an experimenter blinded to the treatment groups. The results of qRT-PCR and Luminex analyses are expressed as mean +/- SEM of at least four independent experiments; the number of analysed samples is indicated in the figure legends or on the graphs. Statistical analysis was done using the non-parametric Mann-Whitney t-test with Graphpad 5.0 software (San Diego, CA, USA). Significance is shown on the graphs (*, $p < 0.05$; **, $p < 0.01$; ***, $p < 0.001$). Specific statistical analyses for ATAC-seq and microarray analyses are detailed in the dedicated sections of Material and Methods. The significance of intersection between the two datasets was evaluated by hypergeometric test (Phyper function) in R studio.

REFERENCES

1. Delobel-Ayoub M, Arnaud C, White-Koning M, Casper C, Pierrat V, Garel M, Burguet A, Roze JC, Matis J, Picaud JC, Kaminski M, Larroque B; EPIPAGE Study Group. Behavioral problems and cognitive performance at 5 years of age after very preterm birth: the EPIPAGE Study. Pediatrics. 2009 Jun;123(6):1485-92. doi: 10.1542/peds.2008-1216. PMID: 19482758Ball G, Boardman JP, Rueckert D, Aljabar P, Arichi T, Merchant N, Gousias IS, Edwards AD, Counsell SJ. The effect of preterm birth on thalamic and cortical development. Cereb Cortex. 2012 May;22(5):1016-24. doi: 10.1093/cercor/bhr176. PMID: 21772018

2. Volpe JJ. Brain injury in premature infants: a complex amalgam of destructive and developmental disturbances. Lancet Neurol. 2009 Jan;8(1):110-24. doi: 10.1016/S1474-4422(08)70294-1. PMID: 19081519

3. Bokobza C, Van Steenwinckel J, Mani S, Mezger V, Fleiss B, Gressens P. Neuroinflammation in preterm babies and autism spectrum disorders. Pediatr Res. 2018 Nov 16. doi: 10.1038/s41390-018-0208-4. [Epub ahead of print] Review. PMID: 30446768

4. Ball G, Boardman JP, Rueckert D, Aljabar P, Arichi T, Merchant N, Gousias IS, Edwards AD, Counsell SJ. The effect of preterm birth on thalamic and cortical development. Cereb Cortex. 2012 May;22(5):1016-24. doi: 10.1093/cercor/bhr176. PMID: 21772018

5. Billiards SS, Haynes RL, Folkerth RD, Borenstein NS, Trachtenberg FL, Rowitch DH, Ligon KL, Volpe JJ, Kinney HC. Myelin abnormalities without oligodendrocyte loss in periventricular leukomalacia. Brain Pathol. 2008 Apr;18(2):153-63. doi: 10.1111/j.1750-3639.2007.00107.x. PMID: 18177464

6. Leviton A, Gressens P. Neuronal damage accompanies perinatal white-matter damage. Trends Neurosci. 2007 Sep;30(9):473-8. PMID: 17765331

7. Hagberg H, Mallard C, Ferriero DM, Vannucci SJ, Levison SW, Vexler ZS, Gressens P. The role of inflammation in perinatal brain injury. Nat Rev Neurol. 2015 Apr;11(4):192-208. doi: 10.1038/nrneurol.2015.13. PMID: 25686754

8. Favrais G, van de Looij Y, Fleiss B, Ramanantsoa N, Bonnin P, Stoltenburg-Didinger G, Lacaud A, Saliba E, Dammann O, Gallego J, Sizonenko S, Hagberg H, Lelièvre V, Gressens P. Systemic inflammation disrupts the developmental program of white matter. Ann Neurol. 2011 Oct;70(4):550-65. doi: 10.1002/ana.22489. PMID: 21796662

9. Krishnan ML, Van Steenwinckel J, Schang AL, Yan J, Arnadottir J, Le Charpentier T, Csaba Z, Dournaud P, Cipriani S, Auvynet C, Titomanlio L, Pansiot J, Ball G, Boardman JP, Walley AJ, Saxena A, Mirza G, Fleiss B, Edwards AD, Petretto E, Gressens P. Integrative genomics of microglia implicates DLG4 (PSD95) in the white matter development of preterm infants. Nat Commun. 2017 Sep 5;8(1):428. doi: 10.1038/s41467-017-00422-w. PMID: 28874660

10. Shiow LR, Favrais G, Schirmer L, Schang AL, Cipriani S, Andres C, Wright JN, Nobuta H, Fleiss B, Gressens P, Rowitch DH. Reactive astrocyte COX2-PGE2 production inhibits oligodendrocyte maturation in neonatal white matter injury. Glia. 2017 Dec;65(12):2024-2037. doi: 10.1002/glia.23212. Epub 2017 Aug 30.

11. Rangon CM, Schang AL, Van Steenwinckel J, Schwendimann L, Lebon S, Fu T, Chen L, Beneton V, Journiac N, Young-Ten P, Bourgeois T, Maze J, Matrot B, Baburamani AA, Supramaniam V, Mallard C, Trottet L, Edwards AD, Hagberg H, Fleiss B, Li J, Chuang TT, Gressens P. Myelination induction by a histamine H3 receptor antagonist in a mouse model of preterm white matter injury. Brain Behav Immun. 2018 Nov;74:265-276. doi: 10.1016/j.bbi.2018.09.017. Epub 2018 Sep 12. PMID: 30218783

12. Buenrostro JD, Giresi PG, Zaba LC, Chang HY, Greenleaf WJ. Transposition of native chromatin for fast and sensitive epigenomic profiling of open chromatin, DNA-binding proteins and nucleosome position. Nat Methods. 2013 Dec;10(12):1213-8. doi: 10.1038/nmeth.2688. PMID: 24097267

13. Yanai H, Negishi H, Taniguchi T. The IRF family of transcription factors: Inception, impact and implications in oncogenesis. Oncoimmunology. 2012 Nov 1;1(8):1376-1386. PMID: 23243601

14. Piper J, Elze MC, Cauchy P, Cockerill PN, Bonifer C, Ott S. Wellington: a novel method for the accurate identification of digital genomic footprints from DNase-seq data. Nucleic Acids Res. 2013 Nov;41(21):e201. doi: 10.1093/nar/gkt850. Epub 2013 Sep 25. Erratum in: Nucleic Acids Res. 2014;42(17):11272. PMID: 24071585

15. Green B, Bouchier C, Fairhead C, Craig NL, Cormack BP. Insertion site preference of Mu, Tn5, and Tn7 transposons. Mob DNA. 2012 Feb 7;3(1):3. doi: 10.1186/1759-8753-3-3. PMID: 22313799

16. Hogan NT, Whalen MB, Stolze LK, Hadeli NK, Lam MT, Springstead JR, Glass CK, Romanoski CE. Transcriptional networks specifying homeostatic and inflammatory programs of gene expression in human aortic endothelial cells. Elife. 2017 Jun 6;6. pii: e22536. doi: 10.7554/eLife.22536. PMID: 28585919

17. Espín-Palazón R, Traver D. The NF-κB family: Key players during embryonic development and HSC emergence. Exp Hematol. 2016 Jul;44(7):519-27. doi: 10.1016/j.exphem.2016.03.010. Epub 2016 Apr 28. PMID: 27132652

18. Abane R, Mezger V. Roles of heat shock factors in gametogenesis and development. FEBS J. 2010 Oct;277(20):4150-72. PMID: 20945531

19. Chang Y, Ostling P, Akerfelt M, Trouillet D, Rallu M, Gitton Y, El Fatimy R, Fardeau V, Le Crom S, Morange M, Sistonen L, Mezger V. Role of heat-shock factor 2 in cerebral cortex formation and as a regulator of p35 expression. Genes Dev. 2006 Apr 1;20(7):836-47. PMID: 16600913

20. Gomez-Pastor R, Burchfiel ET, Thiele DJ. Regulation of heat shock transcription factors and their roles in physiology and disease. Nat Rev Mol Cell Biol. 2018 Jan;19(1):4-19. doi: 10.1038/nrm.2017.73. Epub 2017 Aug 30. Review. PMID: 28852220

21. Zeis T, Enz L, Schaeren-Wiemers N. The immunomodulatory oligodendrocyte. Brain Res. 2016 Jun 15;1641(Pt A):139-148. doi: 10.1016/j.brainres.2015.09.021. Epub 2015 Sep 28. PMID: 26423932

22. Kang Z, Wang C, Zepp J, Wu L, Sun K, Zhao J, Chandrasekharan U, DiCorleto PE, Trapp BD, Ransohoff RM, Li X. Act1 mediates IL-17-induced EAE pathogenesis selectively in NG2+ glial cells. Nat Neurosci. 2013 Oct;16(10):1401-8. doi: 10.1038/nn.3505. Epub 2013 Sep 1. PMID: 23995070

23. Cahoy JD, Emery B, Kaushal A, Foo LC, Zamanian JL, Christopherson KS, Xing Y, Lubischer JL, Krieg PA, Krupenko SA, Thompson WJ, Barres BA. A transcriptome database for astrocytes, neurons, and oligodendrocytes: a new resource for understanding brain development and function. J Neurosci. 2008 Jan 2;28(1):264-78. doi: 10.1523/JNEUROSCI.4178-07.2008. PMID: 18171944

24. Kumar H, Lim JH, Kim IS, Choi DK. Differential regulation of HIF-3α in LPS-induced BV-2 microglial cells: Comparison and characterization with HIF-1α. Brain Res. 2015 Jun 12;1610:33-41. doi: 10.1016/j.brainres.2015.03.046. Epub 2015 Apr 3. PMID: 25847716

25. Cuomo F, Coppola A, Botti C, Maione C, Forte A, Scisciola L, Liguori G, Caiafa I, Ursini MV, Galderisi U, Cipollaro M, Altucci L, Cobellis G. Pro-inflammatory cytokines activate hypoxia-inducible factor 3α via epigenetic changes in mesenchymal stromal/stem cells. Sci Rep. 2018 Apr 11;8(1):5842. doi: 10.1038/s41598-018-24221-5. PMID: 29643458

26. West JA, Cook A, Alver BH, Stadtfeld M, … Park PJ, Tolstorukov MY, Kingston RE. Nucleosomal occupancy changes locally over key regulatory regions during cell differentiation and reprogramming. Nat Commun 2014 5:4719. PMID: 25158628.

27. Stadhouders R, Vidal E, Serra F, Di Stefano B, Le Dily F, Quilez J, Gomez A, Collombet S, Berenguer C, Cuartero Y, Hecht J, Filion GJ, Beato M, Marti-Renom MA, Graf T. Transcription factors orchestrate dynamic interplay between genome topology and gene regulation during cell reprogramming. Nat Genet. 2018 Feb;50(2):238-249. doi: 10.1038/s41588-017-0030-7. Epub 2018 Jan 15. PMID: 29335546

28. Barnett ML, Tusor N, Ball G, Chew A, Falconer S, Aljabar P, Kimpton JA, Kennea N, Rutherford M, David Edwards A, Counsell SJ. Exploring the multiple-hit hypothesis of preterm white matter damage using diffusion MRI. Neuroimage Clin. 2017 Nov 21;17:596-606. doi: 10.1016/j.nicl.2017.11.017. eCollection 2018. PMID: 29234596

29. Volpe JJ. Systemic inflammation, oligodendroglial maturation, and the encephalopathy of prematurity. Ann Neurol. 2011 Oct;70(4):525-9. doi: 10.1002/ana.22533. PMID: 22028217

30. Moyon S, Dubessy AL, Aigrot MS, Trotter M, Huang JK, Dauphinot L, Potier MC, Kerninon C, Melik Parsadaniantz S, Franklin RJ, Lubetzki C. Demyelination causes adult CNS progenitors to revert to an immature state and express immune cues that support their migration. J Neurosci. 2015 Jan 7;35(1):4-20. doi: 10.1523/JNEUROSCI.0849-14.2015. PMID: 25568099

31. Vela JM, Molina-Holgado E, Arévalo-Martín A, Almazán G, Guaza C. Interleukin-1 regulates proliferation and differentiation of oligodendrocyte progenitor cells. Mol Cell Neurosci. 2002 Jul;20(3):489-502. PMID: 12139924

32. Jana M, Pahan K. Redox regulation of cytokine-mediated inhibition of myelin gene expression in human primary oligodendrocytes. Free Radic Biol Med. 2005 Sep 15;39(6):823-31. PMID: 16109311

33. Balabanov R, Strand K, Goswami R, McMahon E, Begolka W, Miller SD, Popko B. Interferon-gamma-oligodendrocyte interactions in the regulation of experimental autoimmune encephalomyelitis. J Neurosci. 2007 Feb 21;27(8):2013-24. PMID: 17314297

34. Schang AL, Van Steenwinckel J, Chevenne D, Alkmark M, Hagberg H, Gressens P, Fleiss B. Failure of thyroid hormone treatment to prevent inflammation-induced white matter injury in the immature brain. Brain Behav Immun. 2014 Mar;37:95-102. doi: 10.1016/j.bbi.2013.11.005. Epub 2013 Nov 12. PMID: 24240022

35. McCarthy KD, de Vellis J. Preparation of separate astroglial and oligodendroglial cell cultures from rat cerebral tissue. J Cell Biol. 1980 Jun;85(3):890-902. PMID: 6248568

36. Pansiot J, Pham H, Dalous J, Chevenne D, Colella M, Schwendimann L, Fafouri A, Mairesse J, Moretti R, Schang AL, Charriaut-Marlangue C, Gressens P, Baud O. Glial response to 17 β -estradiol in neonatal rats with excitotoxic brain injury. Exp Neurol. 2016 Aug;282:56-65. doi: 10.1016/j.expneurol.2016.05.024. Epub 2016 May 21. PMID: 27222132

37. Jung M, Krämer E, Grzenkowski M, Tang K, Blakemore W, Aguzzi A, Khazaie K, Chlichlia K, von Blankenfeld G, Kettenmann H, et al. Lines of murine oligodendroglial precursor cells immortalized by an activated neu tyrosine kinase show distinct degrees of interaction with axons in vitro and in vivo. Eur J Neurosci. 1995 Jun 1;7(6):1245-65. PMID: 7582098

38. Gobert RP, Joubert L, Curchod ML, Salvat C, Foucault I, Jorand-Lebrun C, Lamarine M, Peixoto H, Vignaud C, Frémaux C, Jomotte T, Françon B, Alliod C, Bernasconi L, Abderrahim H, Perrin D, Bombrun A, Zanoguera F, Rommel C, Hooft van Huijsduijnen R. Convergent functional genomics of oligodendrocyte differentiation identifies multiple autoinhibitory signaling circuits. Mol Cell Biol. 2009 Mar;29(6):1538-53. doi: 10.1128/MCB.01375-08. Epub 2009 Jan 12. PMID: 19139271

39. Chhor V, Le Charpentier T, Lebon S, Oré MV, Celador IL, Josserand J, Degos V, Jacotot E, Hagberg H, Sävman K, Mallard C, Gressens P, Fleiss B. Characterization of phenotype markers and neuronotoxic potential of polarised primary microglia in vitro. Brain Behav Immun. 2013 Aug;32:70-85. doi: 10.1016/j.bbi.2013.02.005. Epub 2013 Feb 27. PMID: 23454862

40. Robinson MD, McCarthy DJ, Smyth GK (2010). “edgeR: a Bioconductor package for differential expression analysis of digital gene expression data.” Bioinformatics **26**(1), 139-140. PMID: 19910308

41. Afgan E, Baker D, van den Beek M, Blankenberg D, Bouvier D, Čech M, Chilton J, Clements D, Coraor N, Eberhard C, Grüning B, Guerler A, Hillman-Jackson J, Von Kuster G, Rasche E, Soranzo N, Turaga N, Taylor J, Nekrutenko A, Goecks J. The Galaxy platform for accessible, reproducible and collaborative biomedical analyses: 2016 update. Nucleic Acids Res. 2016 Jul 8;44(W1):W3-W10. doi: 10.1093/nar/gkw343. PMID: 27137889

42. Huang da W, Sherman BT, Lempicki RA. Systematic and integrative analysis of large gene lists using DAVID bioinformatics resources. Nat Protoc. 2009;4(1):44-57. doi: 10.1038/nprot.2008.211. PMID: 19131956

43. Huang da W, Sherman BT, Lempicki RA. Bioinformatics enrichment tools: paths toward the comprehensive functional analysis of large gene lists. Nucleic Acids Res. 2009 Jan;37(1):1-13. doi: 10.1093/nar/gkn923. Epub 2008 Nov 25. PMID: 19033363

LEGENDS OF FIGURES

Figure 1. Experimental strategy. Previously validated mouse model of encephalopathy of prematurity in which we mimic the systemic and neuroinflammatory insults as undergone by human infants from approximately 23-32 weeks gestational age equivalent. Neuroinflammation is induced *via* i.p. IL1B from postnatal days 1 to 5, and this leads to OPC maturation blockade, defective myelination, and behavioral anomalies as seen clinically (8). O4+ OPCs (green circles) were isolated from P5 pup cortices by MACS and genome-wide chromatin accessibility was explored by ATAC-Seq (lower, left panel): the enzymatic severing of the DNA by the transposome (Tn5 transposase, loaded with adapters *in vitro*; green and orange) allows « tagmentation » of DNA template, to fragments tagged with adapters. In parallel (lower, right panel), comparative transcriptomic analysis was performed using Agilent mouse whole genome microarray.

Figure 2. The epigenome of OPCs is mostly unchanged after IL1B treatment as assessed by ATAC-Seq analysis of chromatin accessibility.

(*A*) PCA analysis of log normalized read counts falling within ATAC-seq chromatin peaks from OPCs from control (PBS) or neuroinflammation-exposed (IL1B injections); total number of peaks, 213,246.

(*B*) Scatter plot representing the dispersion (fold change) of peaks in relation to the number of *reads* (logCPM), for each individual analyzed peak across 3 PBS samples and 3 IL1B samples. The 524 peaks showing significant differences between IL1B and PBS conditions are indicated in red, with 391 peaks corresponding to increased and 134 peaks to decreased chromatin accessibility, with FDR < 0.05.

(*C*) Heat map visualization of the 524 opening (yellow) or closing (blue) peaks in control (PBS) and neuroinflammation-exposed (IL1B injected) conditions.

(*D*) Examples of peaks showing increased chromatin accessibility: (Upper and middle panels) peak located at the most downstream position in the *Hif3a gene* (*Hypoxia inducible factor 3 alpha subunit;* magnification in the middle panel). Example of peak without significant changes in chromatin accessibility: (Upper panel) the peak located in the middle of the *Hif3a* gene illustrated region. Example of peak showing reduced chromatin accessibility: (Lower panel) peaks within the *Cwc22* gene (encoding the spliceosome-associated protein 22).

Figure 3. The top 5 most upregulated pathways due to neuroinflammatory-exposure comprise genes of the immune system and inflammatory response pathways (see Table S4)**.** Microarray analysis comparing gene expression in isolated O4+ OPCs from six independent control (PBS) and six independent neuroinflammation-exposed cortices (IL1B; Fig. 1).

(*A*) **Heat map of genes with altered expression upon IL1B exposure.** A fold-change (FC) threshold of +/-1.5 was chosen, with FDR < 0.05. Total number of probes corresponding to IL1B-induced disturbances in gene expression: 2571, corresponding to 1719 genes. Total number of probes corresponding to the 1266 upregulated genes: 1872. Total number of probes corresponding to the 454 downregulated genes: 699. Heatmap color scale: log2 [-2.0;+2.0].

(*B*) **The top5 GO of up-regulated genes corresponds to the immune system and inflammatory response pathways**. GO-terms as a table with p-values and FDR.

(*C*) **Heat map of the genes belonging to the top5 GO-terms,** 315 probes corresponding to 262 genes. Heatmap color scale: log2 [-2.0;+2.0].

(*D*) **Validation of the alteration in gene expression for members of the GO-term "immune system and inflammatory response pathways" in O4+ OPCs using RT-qPCR**. Number of independent experiments: n=8 for all genes, except for *Cxcl9*, *Cxcl10*, and *Il1r1* (n=7).*, p < 0.05; **, p < 0.01; ***, p < 0.001. Grey bars ligands; black bars: receptors.

Figure 4. The induction in cytokine and chemokine expression by exposure to neuroinflammation in OPCs at P5 is not due to contamination by microglia (CD11B+) or astrocytes (GLAST+)

(*A*) A heatmap comparing the microarray data of the 262 genes upregulated of the inflammatory pathway in isolated O4+ OPCs in response to neuroinflammation, with the same genes from isolated CD11+ microglial cells (9) at the same timepoint. These 262 genes are not dysregulated in a comparable way in these two cell types. Heatmap color scale of log2 [-2.0;+2.0].

(*B*) Unique signature for inflammatory gene expression in isolated O4+ OPCs, compared to CD11B+ microglia, and GLAST+ astrocytes. Fold-change in the expression of genes of the immune and inflammatory pathways as detected by RT-qPCR analyses at different postnatal stages. mRNA levels are normalized to *Gapdh* for OPCs and astrocytes and *Rpl13* for microglia based on in-house reference gene testing. The numbers of independent experiments are indicated on each plot. *, $p < 0.05$; **, $p < 0.01$; ***, $p < 0.001$.

Figure 5. The production of cytokine and chemokine proteins is induced by exposure of MACS-isolated O4+ OPCs, to IL1B ***ex vivo***

(*A*) Experimental design for *ex vivo* OPC culture, inflammatory exposure (IL1B), and differentiation (see Material and Methods).

(*B*) Detection and quantification (pG/mL) of the expression of interleukins (IL1B, IL6), cytokine C-C Motif Chemokine Ligand 2, 4, and 5 proteins (CCL2, CCL3, CCL4, and CCL5) and chemokine C-X-C Motif Chemokine Ligand 2 (CXCL2) proteins by Luminex. CTR, PBS exposure; IL1B, IL1B exposure. The dotted line represents the limit of detection for individual proteins in the assay. The numbers of independent experiments performed for each plot are indicated on each plot. *, $p < 0.05$; **, $p < 0.01$; ***, $p< 0.001$.

Figure 6. Crosstabulation of ATAC-Seq and microarray data reveals major involvement of TFs of the immune and inflammatory pathways in O4+ OPCs.

(*A*) **Number of genes differentially expressed and associated with all differentially accessible peaks**/regions in O4+ OPCs isolated from neuroinflammation-exposed pups.

(*B*) **Number of genes differentially expressed and associated with differentially accessible peaks/regions only located +/- 8 kb around their TSS** in O4+ OPCs isolated from neuroinflammation-exposed pups.

(*C*) **Heat map illustrating the co-localization of pairs of TF binding motifs** in the 2319 ATAC-Seq peaks located within +/- 8 kb from the TSS 1266 upregulated genes (corresponding to 886 different gene names), identified using paired motif analysis. TF names from MEME nomenclature on both axes. Statistically relevant co-occurrence of two different TFs is indicated by yellow to orange squares (multiple testing corrected log10 p-value). Examples of TF pairs are indicated IRF1-p50; *ISRE*-p65; PU.1-IRF8-p65; PU.1-iRF8-p50; PU.1-BATF; PU.1-FOSL2. Color code (TF names and arrows): red, pairing of PU.1-IRF8 with NFκB subunit binding motifs; purple, pairing of PU.1 with AP-1 family binding motifs; blue, pairing of NFKB binding motifs with *Isre* (IFN-stimulated response element); green, pairing of NFKB with IRF binding motifs.

(*D*) **Examples of chromatin accessibility footprints at TF motifs:** average footprint profiles at TF motifs were plotted at base pair resolution, located within accessible chromatin *loci* in <u>both</u> PBS and IL1B conditions, adjacent to differentially regulated genes (ALL; down and upregulated) using the Wellington software (14). Typical footprint profiles coincide with the center of the canonical motif for a given TF (indicated by brackets). Footprints for occupancy of IRF1, IRF2, *Isre,* and NFκB binding motifs are illustrated. Footprints showing occupancy by IRF1, IRF2, *Isre,* and NFκB on corresponding binding motifs are illustrated. Red and blue curves: + and - strand, respectively.

Figure 7. Constitutive expression of genes encoding cytokines and chemokines at early stages of normal (unstressed) O4+ OPC maturation.

(*A*) RT-qPCR analyses in P3, P5, and P10 O4+ OPCs. N= 5 to 6 independent experiments. Two-way ANOVA followed by Bonferroni - Post Hoc Test was performed: * and +, $p < 0.05$; ** and, ++ $p < 0.01$; ***, $p < 0.001$. *, **, or ***, correspond to comparison between PBS and IL1 conditions for a given postnatal stage; + (or ++), correspond to comparison between P5 (or P10) to P3.

(*B*) RT-qPCR analyses in the Oli-neu cell line before or after 72 hours of differentiation triggered by PD174265, a potent, cell-permeable inhibitor of the tyrosine kinase activity of the epidermal growth factor receptor (EGFR). This *in vitro* paradigm shows the same pattern of higher inflammatory mediator expression in immature oligodendrocytes, which decreases with maturation to myelin producing oligodendrocytes. Numbers of independent experiments are indicated on the graph bars. *, $p < 0.05$; **, $p < 0.01$. nd: not detected.

(*C*) **Cross-species comparison reveals presence of an inflammation-like signature in the chromatin landscape of**

both control and IL1B treated O4+ OPC samples. Read number distribution of peaks upon IL1B treatment in the HAEC (public) and OPC datasets. Reads were normalized for each set of peaks against the total number of reads present in all (7,739) matched peaks and converted into reads per million. Distributions were compared using a one-sample Wilcoxon rank test.

LEGENDS OF SUPPLEMENTAL FIGURES

Figure S1. (related to Fig. 1).

(*A*) **Quality assessment of the O4+ OPC cell purification process**. RT-qPCR experiments on the O4+ OPC, CD11+ microglia (9), (3 PBS samples and 3 IL1B samples) and unlabeled cell populations, showing that, in contrast to microglia and astrocytes (unlabeled), O4+ OPCs, used in this study, express the *Mbp* gene, but very low mRNA levels of the microglia marker CD11 (encoded by the *Itgam* gene), the astrocyte marker *Gfap*, or of the neuronal marker *NeuN*. Note that *NeuN* is very lowly expressed, even in the unlabeled population, which mainly contains astrocytes, because neurons poorly survive our MACS protocol.

(*B*) **Validation of OPC maturation arrest in the model. RT-qPCR analysis of the expression of myelination and progenitor markers in OPCs**.

Myelin markers: *Mbp*, Myelin binding protein; *Mog*, Myelin oligodendrocyte glycoprotein; *Mag*, Myelin-associated glycoprotein. *Plp1*, proteolipid protein 1, a transmembrane, predominant component of myelin; *Cnp*, 2',3'-Cyclic Nucleotide 3' Phosphodiesterase, abundant protein in myelin in the central nervous system. Progenitor (OPC) markers: *Id2*, Inhibitor of differentiation 2; *Pdgfra*, Platelet Derived Growth Factor Receptor Alpha, a marker of OPCs. Number of independent experiments: n = 7 for *Cnp*, *Mag*, and *Pdgfra*; and n = 15 for *Mbp*, *Mog*, and *Id2*. ns: not statistically significant; *, $p < 0.05$; ***, $p < 0.001$.

(*C*) **Schematic representation of the bioinformatics and statistics workflow used for the analysis of ATAC-Seq data**

(*D*) **Fragment length distributions in ATAC-Seq samples**. Insert size distribution shows visible large periodicity of the nucleosome-free, mononucleosomal and dinucleosomal fragments, as well as the expected ~10.4bp periodicity, resulting from steric hindrance of the helical twist of the DNA on the nucleosome surface.

Figure S2. The epigenome of OPCs is mostly unchanged after IL1B treatment as assessed by ATAC-Seq analysis of chromatin accessibility (related to Fig. 2).

(*A*) Multidimensional Scaling (MDS) plot of distances between the 3 PBS samples and the 3 IL1B samples, using EdgeR.

(*B*) Scatter plots representing the dispersion (logfold change) as the number of *reads* (logCPM), for each individual analyzed peak (across 3 PBS samples and 3 IL1B samples). In red, peaks showing differential chromatin accessibility with FDR < 0.05. The upper left plot is identical to Fig 2*B* and is included here for comparison. Upper right, lower left, and lower right: scatter plots for analyses with permuted sample labels, created by swapping of one of the PBS samples with one other IL1B samples or, vice-versa. Mixing PBS and IL1B samples led to very reduced numbers of differential peaks, confirming that differential peaks found with correct sample labels are not statistical artefacts

(*C*) Distribution of the total number of peaks and of the 524 differential open peaks (right-hand side) in various genomic regions.

(*D*) Examples of peaks showing reduced or unchanged chromatin accessibility: the cytokine C-C Motif Chemokine Ligand 2 gene (*Ccl2*; upper panel), or *C-X-C Motif Chemokine Ligand 1* and *10* genes *(Cxcl1* or *Cxcl10; Lower panels)*, respectively.

(*E*) GO analysis, using DAVID6.8, using genes with TSS that is annotated with one or more differentially accessible chromatin regions (total of 524 ATAC-Seq peaks).

Figure S3. (related to Fig. 3).

(*A*) **Quality control of the samples used for microarray analysis.** Microarray analysis of fold change (FC) in gene expression of myelin markers that start to be expressed at P5 and of OPC markers.

(*B*) **GO analysis corresponding to the TOP-10 genes, downregulated upon IL1B treatment, using DAVID6.8**.

Figure S4. Heat maps of the overall comparison of IL1B-induced perturbations in gene expression in isolated O4+ OPCs and CD11+ microglial cells. (related to Fig. 4). OP4+ OPCs exhibit profiles of transcriptomic modifications globally very different from that of CD11+ microglial cells. Examples of genes encoding cytokines and chemokines are pointed out by rectangles. Most of them are not upregulated in CD11+ microglial cells at P5, in contrast to what happens in O4+ OPCs. Fold change ([-2.0; +2.0]; IL1B/PBS).

Figure S5. (related to Fig. 5 and Fig. 6).

(*A*) **The induction of cytokine and chemokine mRNA levels, upon IL1B exposure, is reproduced in MACS-isolated *ex vivo* cultured OPCs during differentiation**. RT-qPCR experiments on OPCs collected after 72h of differentiation. Number of independent experiments: n = 6 per condition (PBS or IL1B). *, $p < 0.05$; **, $p < 0.01$; ***, $p < 0.01$.

(*B*) TFBS motifs identified in significant ATAC-seq peaks adjacent to differentially regulated genes, using HOMER known motifs.

(*C*) TFBS motifs identified in significant ATAC-seq peaks adjacent to upregulated genes, using HOMER known motifs.

Figure S6. Examples of chromatin accessibility footprint profiles at TF motifs. (related to Fig. 6). Average footprint profiles at TF motifs plotted at base pair resolution, located within accessible chromatin *loci* adjacent to any differentially regulated genes (down or upregulated) for the following TF or binding site (*A*): *Isre,* IRF1, IRF2, NFκB in PBS-treated or IL1B-treated samples, indicating that these TFs might already bind DNA. (*B*) for PU.1-IRF8 or PGR factors, from PBS-treated, IL1B-treated samples or from both conditions (PBS plus IL1B), the average footprints showing sharp internal spikes are suggestive of transposase insertion bias.

Figure S7. Constitutive expression of cytokines and chemokines by unstressed early maturating OPCs and subsequent decrease. (related to Fig. 7).

(*A*) RT-qPCR analyses in P3, P5, and P10 O4+ OPCs showing the expected increase in the expression of genes associated with myelination between P5 and P10 in normal conditions and expected impairment of this increase upon IL1B exposure. Note that in this set of experiments the downregulation of myelination genes was not observed at P5, a stage at which these genes only start to be expressed.

(*B*) RT-qPCR experiments comparing O4+ OPC from naïve (no injection), PBS-injected and IL1B-injected pups, showing that PBS injection does not induce expression of cytokines and chemokine genes, since transcripts levels are equivalent in both PBS and naïve conditions, in contrast to what is observed upon IL1B treatment.

(*C*) RT-qPCR analyses in the Oli-neu cell line before or after 72 hours of differentiation triggered by exposure to conditioned medium from primary neuron culture.

(*D*) **Cross-species comparison confirms global similarities in the chromatin landscapes of HAEC and O4+ OPC datasets.** Read number distribution of peaks upon IL1B treatment in the HAEC and OPC datasets. Reads were normalized for each set of peaks against the total number of reads present in the 7,739 matched peaks and converted into reads per million.

LIST AND LEGENDS OF TABLES

TABLES:

Table S1: Alignment statistics of ATAC-seq

The alignment statistics of the samples is in line with what is expected from ATAC-Seq samples. Losing in the region of 10% of reads to mitochondrial alignment is normal for this type of data.

Table S2: Coordinates of the 213,246 peaks (mm10) detected in PBS and/or IL1B samples

MACS2 peak calling was run separately on PBS and IL1B pooled samples (n=3/group). The two resulting peak files (almost 200,000 peaks in each condition) were merged and the mm10 blacklist removed, leading to a list of 213,246 peaks detected in at least one condition (mm10 coordinates).

Table S3: List and annotation of the 524 differentially accessible peaks

Reads were counted in each of the 213,246 peaks (Table S2) for each sample individually (3 PBS and 3 IL1B samples). Comparison and statistical analysis with EdgeR (exact test and FDR by Benjamini-Hochberg method) identified 524 peaks with differential accessibility (FDR<0.05). Peaks were annotated using HOMER annotatePeaks.

Table S4: GO-term Biological Pathway analysis of the 524 differentially accessible peaks

GO-term Biological Pathway enrichment analysis was performed on the list of gene names (478) associated with the 524 peaks (Table S3) using David6.8.

Table S5: List of the differentially expressed probes from the microarray analysis

Agilent microarray data from 6 PBS and 6 IL1B samples (O4+, P5) were submitted to t-test and FDR by Benjamini-Hochberg method. Probes with FDR<0.05 and FC>1.5 (or <-1.5) are listed in the table (Sheet 1). Up-regulated (Sheet 2) and down-regulated (sheet 3) probes are also presented separately. Red flags (columns F and G) indicate the number of undetectable samples (0 means that all samples were detected). Red and green fold change values (column K) correspond to FC>2.0 and FC<-2.0, respectively. Individual values (N to Y columns) are normalized median-centered Log2 intensities.

Table S6: GO-term Biological Pathway analysis of the UP and DOWN-regulated genes

GO-term Biological Pathway enrichment analysis was performed using David6.8 on significantly up-regulated (Sheet 1) and down-regulated genes (Sheet 2) from the microarray analysis (Table S5).

Table S7: Genes whose alterations in expression correlate to opening or closing of the chromatin

Table S8: Genes whose alterations in expression correlate to opening or closing of the chromatin in region located +/- 8kb around the TSS.

Table S9: ATAC-Seq peaks associated with upregulated genes and revealing the existence of paired TFBS motifs

Table S10: Hogan (HAECS) (list of human gene names and the corresponding orthologue genes in mice, that have been used for the cross-species comparison.

Table S11: List of the RT-qPCR primers

ACKNOWLEDGEMENTS

We are grateful to Dr. Kevin Cheeseman (UMR7216) for helpful discussions and comments on the manuscript. This work benefited from equipment and services from the iGenSeq core facility, at the Institut du Cerveau et de la Moëlle (Paris, France). We are particularly grateful to Yannick Marie, the Head of iGenSeq core facility) and Emeline Mundwiller. We are grateful to Dr Sheila Harroch (Pasteur Institute, Paris, France) for the kind gift of the Oli-neu cell line. The authors acknowledge the support of the Freiburg Galaxy Team.

Figure 1

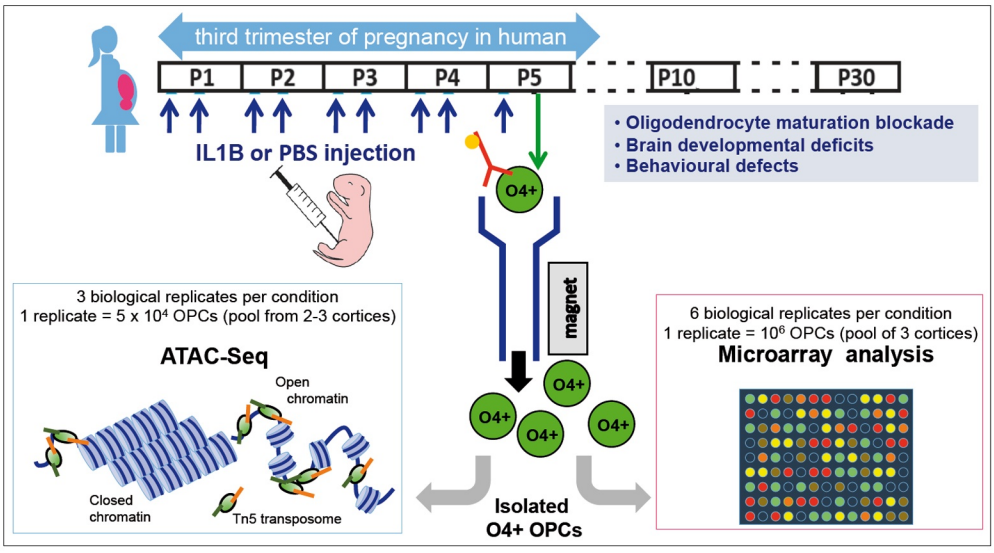
third trimester of pregnancy in human
P1
P2
P3
P4
P5
P10
P30
IL1B or PBS injection
• Oligodendrocyte maturation blockade
• Brain developmental deficits
• Behavioural defects
O4+
magnet
3 biological replicates per condition
1 replicate = 5 x 10⁴ OPCs (pool from 2-3 cortices)
ATAC-Seq
Open chromatin
Closed chromatin
Tn5 transposome
Isolated O4+ OPCs
6 biological replicates per condition
1 replicate = 10⁶ OPCs (pool of 3 cortices)
Microarray analysis

Figure S1

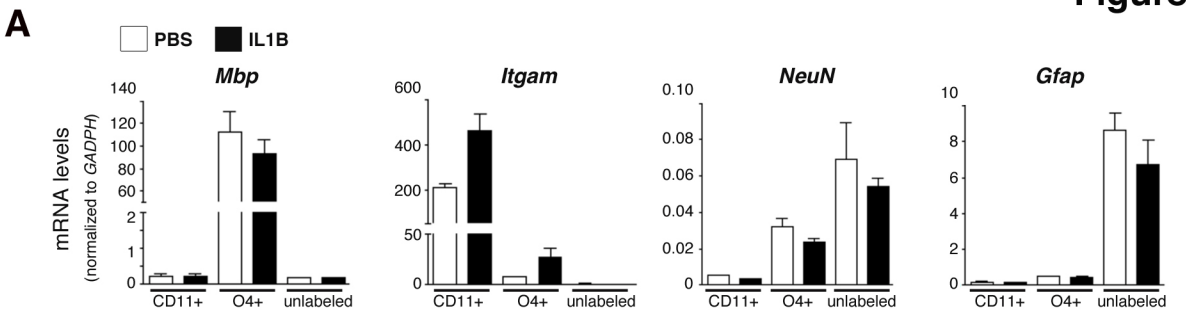
A
PBS
IL1B
Mbp
Itgam
NeuN
Gfap
mRNA levels
(normalized to GADPH)
CD11+
O4+
unlabeled

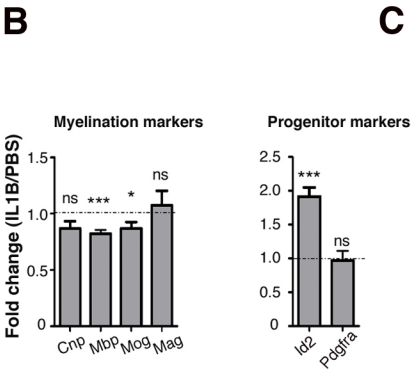
B
Myelination markers
Progenitor markers
Fold change (IL1B/PBS)
ns
***
*
Cnp
Mbp
Mog
Mag
Id2
Pdgfra

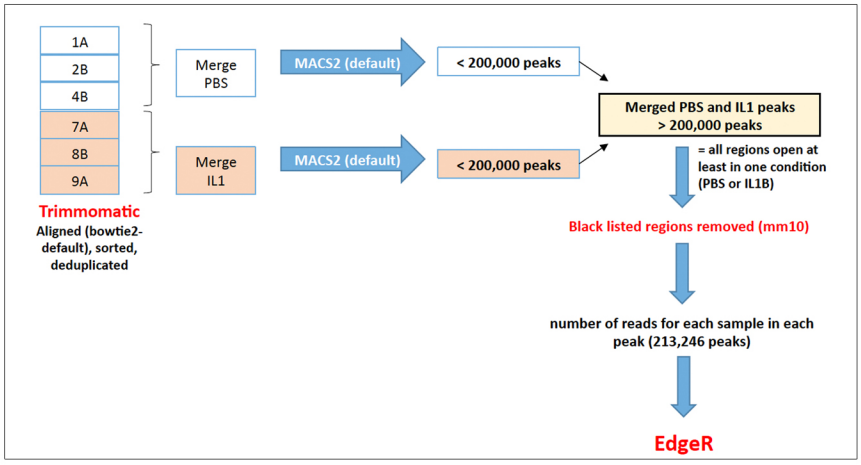
C
1A
2B
4B
7A
8B
9A
Merge PBS
Merge IL1
MACS2 (default)
MACS2 (default)
< 200,000 peaks
< 200,000 peaks
Merged PBS and IL1 peaks > 200,000 peaks
= all regions open at least in one condition (PBS or IL1B)
Black listed regions removed (mm10)
number of reads for each sample in each peak (213,246 peaks)
EdgeR
Trimmomatic
Aligned (bowtie2-default), sorted, deduplicated

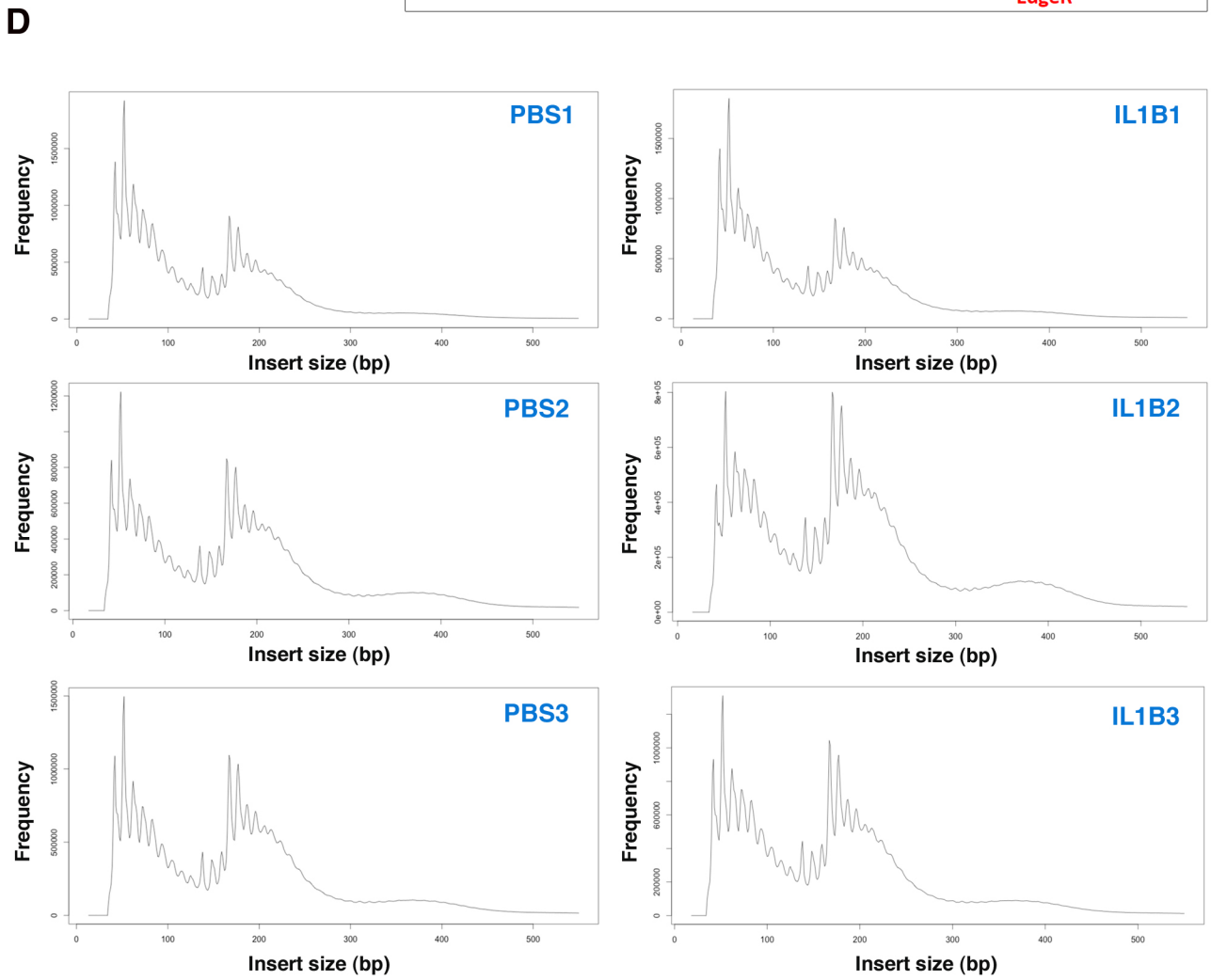
D
PBS1
IL1B1
PBS2
IL1B2
PBS3
IL1B3
Frequency
Insert size (bp)

Figure 2

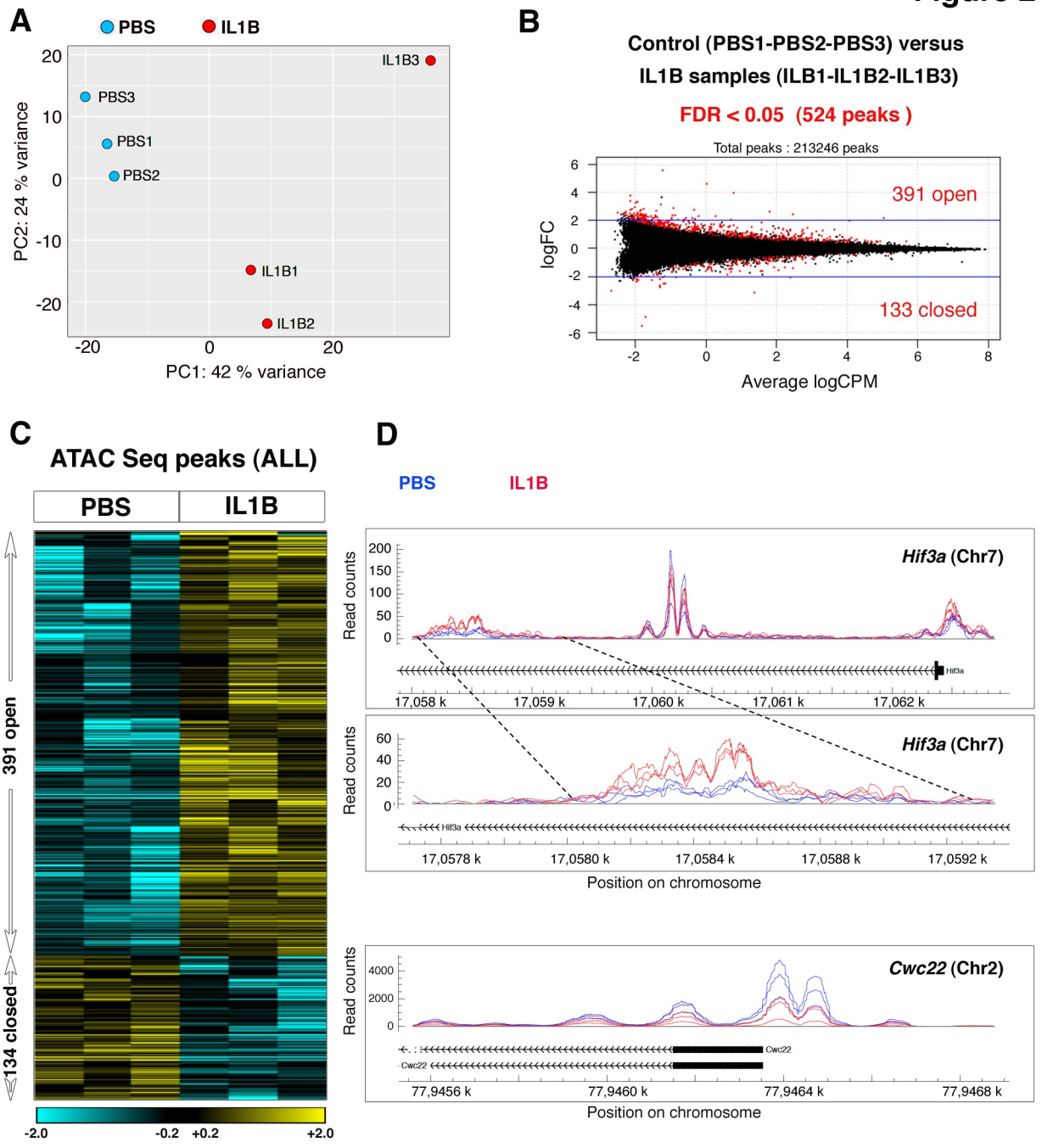
A
PBS
IL1B
PBS3
PBS1
PBS2
IL1B3
IL1B1
IL1B2
PC2: 24 % variance
PC1: 42 % variance
B
Control (PBS1-PBS2-PBS3) versus
IL1B samples (ILB1-IL1B2-IL1B3)
FDR < 0.05 (524 peaks)
Total peaks : 213246 peaks
391 open
133 closed
logFC
Average logCPM
C
ATAC Seq peaks (ALL)
PBS
IL1B
391 open
134 closed
-2.0
-0.2
+0.2
+2.0
D
PBS
IL1B
Hif3a (Chr7)
Read counts
Position on chromosome
Cwc22 (Chr2)

Figure S2

A

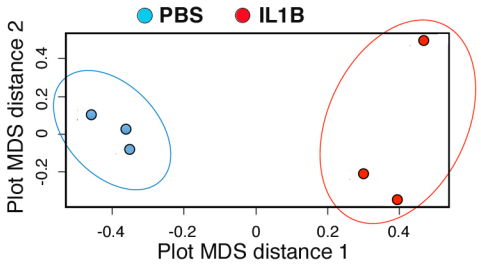

B

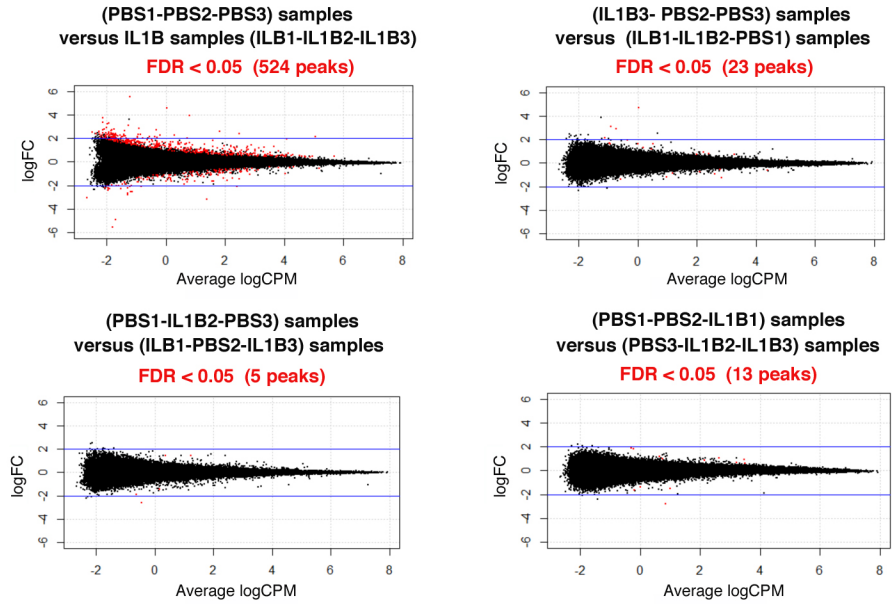

C

	nb of peaks	total size (bp)	log2 Enricht	diff peaks	log2 enricht
intron	105 004	920 840 703	0.541	225	0.344
intergenic	85 643	1 689 213 830	-0.628	258	-0.334
promoter	9 566	27 770 920	2.136	17	1.669
exon	5 945	33 107 990	1.196	9	0.497
TTS	2 550	25 764 803	0.337	6	0.274
3UTR	2 145	19 351 208	0.5	6	0.687
5UTR	1 839	2 048 265	3.518	1	1.342
ncRNA	504	2 599 365	1.307	1	0.998
pseudogene	49	515 405	0.279	1	3.333
snoRNA	1	19	9.392	0	-9.0033
rRNA	0	5 631	-17.702	0	-9.0033
miRNA	0	5 073	-17.702	0	-9.0033

D

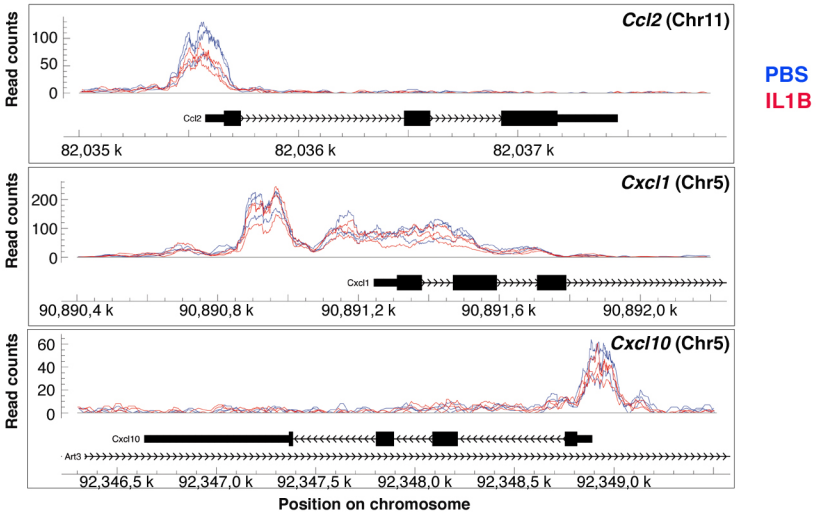

E

Category	Term	Count	Pvalue	Fold Enrichment	FDR
GOTERM_BP_DIRECT	GO:0030335~positive regulation of cell migration	12	1.77E-03	3.11E+00	2.96E+00
GOTERM_BP_DIRECT	GO:0042267~natural killer cell mediated cytotoxicity	4	2.11E-03	1.05E+01	3.52E+00
GOTERM_BP_DIRECT	GO:0007155~cell adhesion	20	2.39E-03	2.17E+00	3.97E+00
GOTERM_BP_DIRECT	GO:0010976~positive regulation of neuron projection development	9	4.86E-03	3.43E+00	7.94E+00
GOTERM_BP_DIRECT	GO:0006857~oligopeptide transport	3	7.07E-03	2.25E+01	1.14E+01
GOTERM_BP_DIRECT	GO:0045862~positive regulation of proteolysis	4	7.97E-03	9.56E+00	1.27E+01
GOTERM_BP_DIRECT	GO:0014850~response to muscle activity	4	9.04E-03	9.14E+00	1.43E+01
GOTERM_BP_DIRECT	GO:0007193~adenylate cyclase-inhibiting G-protein coupled receptor signaling pathway	5	1.03E-02	5.84E+00	1.61E+01
GOTERM_BP_DIRECT	GO:0048681~negative regulation of axon regeneration	3	1.18E-02	1.75E+01	1.83E+01
GOTERM_BP_DIRECT	GO:0006094~gluconeogenesis	4	1.27E-02	8.09E+00	1.95E+01

Figure 3

A

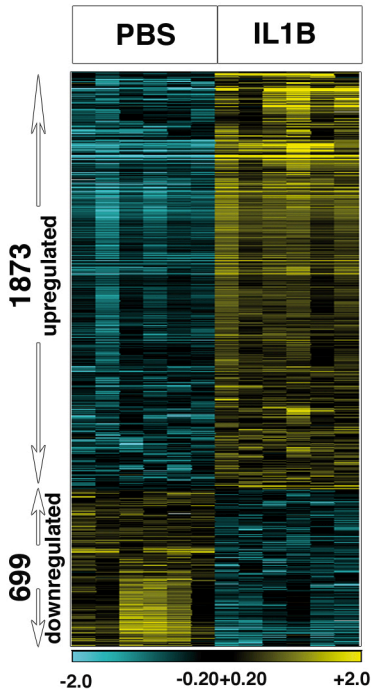

B

Category	Term	Count	PValue	Fold Enrichment	FDR
GOTERM_BP_	GO:0002376~immune system process	128	9.06E-69	6.47E+00	1.67E-65
GOTERM_BP_	GO:0006954~inflammatory response	105	8.35E-52	5.91E+00	1.54E-48
GOTERM_BP_	GO:0045087~innate immune response	102	1.89E-42	4.94E+00	3.48E-39
GOTERM_BP_	GO:0006955~immune response	69	1.64E-28	4.91E+00	3.03E-25
GOTERM_BP_	GO:0006935~chemotaxis	38	1.10E-19	6.23E+00	2.03E-16
GOTERM_BP_	GO:0051607~defense response to virus	42	2.20E-17	4.87E+00	4.06E-14
GOTERM_BP_	GO:0035458~cellular response to interferon-beta	21	1.44E-15	9.92E+00	2.66E-12
GOTERM_BP_	GO:0032496~response to lipopolysaccharide	42	1.25E-14	4.13E+00	2.31E-11
GOTERM_BP_	GO:0071222~cellular response to lipopolysaccharide	43	2.14E-14	3.98E+00	3.93E-11
GOTERM_BP_	GO:0050830~defense response to Gram-positive bacterium	28	9.00E-14	5.83E+00	1.66E-10

C

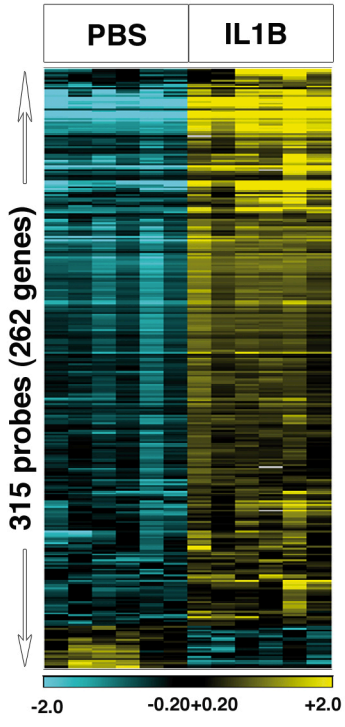

D

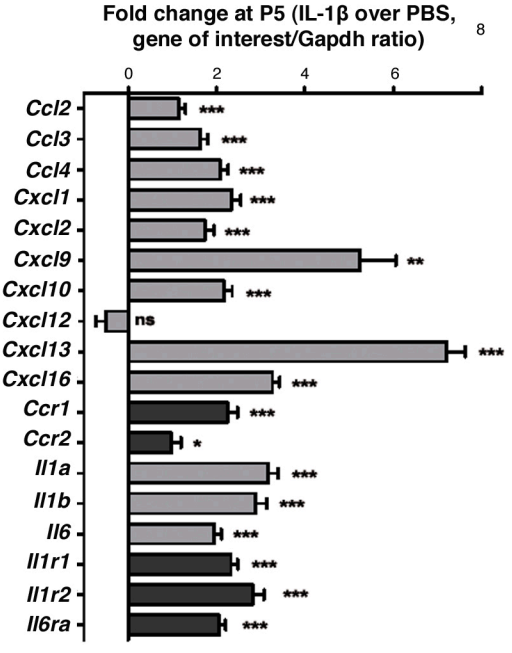

Figure S3

A

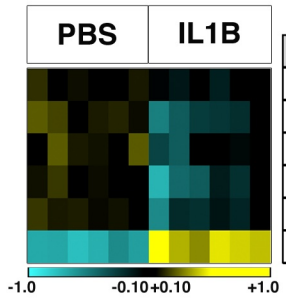

Gene	ReporterID	FC	FDR	
Mbp	A_52_P604195	-1,14	**2,51E-02**	Markers
Mbp	A_52_P329451	-1,42	**2,15E-03**	
Mog	A_66_P123582	-1,21	**1,07E-02**	Myelination
Mag	A_55_P2062757	-1,38	**1,27E-02**	
Plp1	A_55_P2069850	-1,33	**3,64E-03**	
Id2	A_52_P240542	**2,82**	**4,48E-06**	Progenitors

B

Category	Term	Count	PValue	old Enrichmen	FDR
GOTERM_BP_	GO:0001525~angiogenesis	24	5.75E-11	5.60E+00	9.79E-08
GOTERM_BP_	GO:0007275~multicellular organism development	47	8.49E-9	2.55E+00	1.45E-05
GOTERM_BP_	GO:0001568~blood vessel development	12	4.92E-08	9.43E+00	8.37E-05
GOTERM_BP_	GO:0001570~vasculogenesis	11	3.34E-07	9.03E+00	5.70E-04
GOTERM_BP_	GO:0000122~negative regulation of transcription from RNA polymerase II promoter	35	3.39E-07	2.68E+00	5.77E-04
GOTERM_BP_	GO:0001945~lymph vessel development	6	2.02E-06	2.58E+01	3.44E-03
GOTERM_BP_	GO:0001569~patterning of blood vessels	8	6.11E-0.6	1.12E+01	1.04E-02
GOTERM_BP_	GO:0007155~cell adhesion	25	7.25E-06	2.88E+00	1.24E02
GOTERM_BP_	GO:0035050~embryonic heart tube development	6	4.55E-05	1.46E+01	7.75E-02
GOTERM_BP_	GO:0072001~renal system development	6	4.55E-05	1.46E+01	7.75E-02

Figure 4

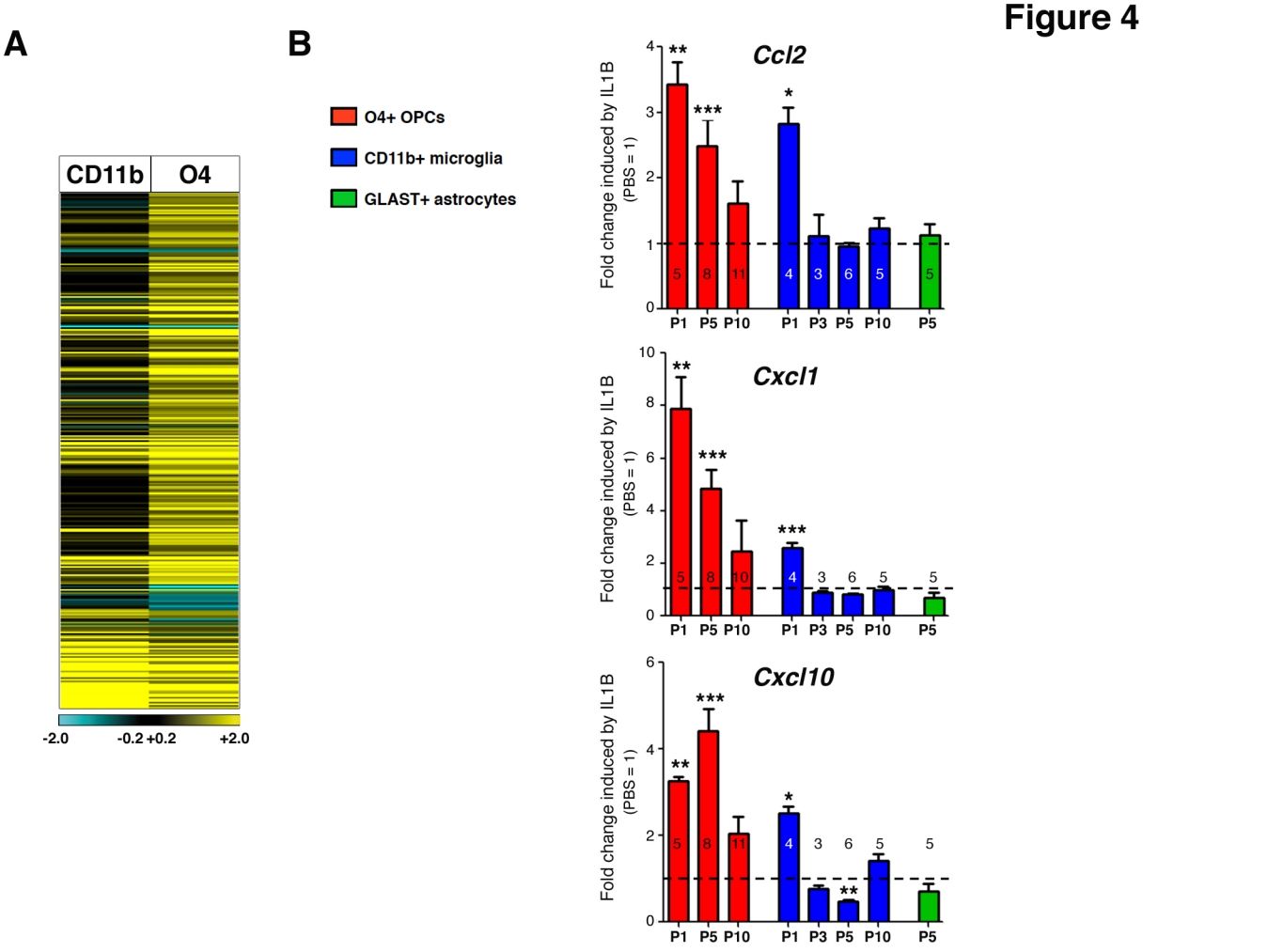
A
CD11b
O4
-2.0
-0.2 +0.2
+2.0
B
O4+ OPCs
CD11b+ microglia
GLAST+ astrocytes
Ccl2
Cxcl1
Cxcl10
Fold change induced by IL1B (PBS = 1)
P1 P5 P10 P1 P3 P5 P10 P5

Figure S4

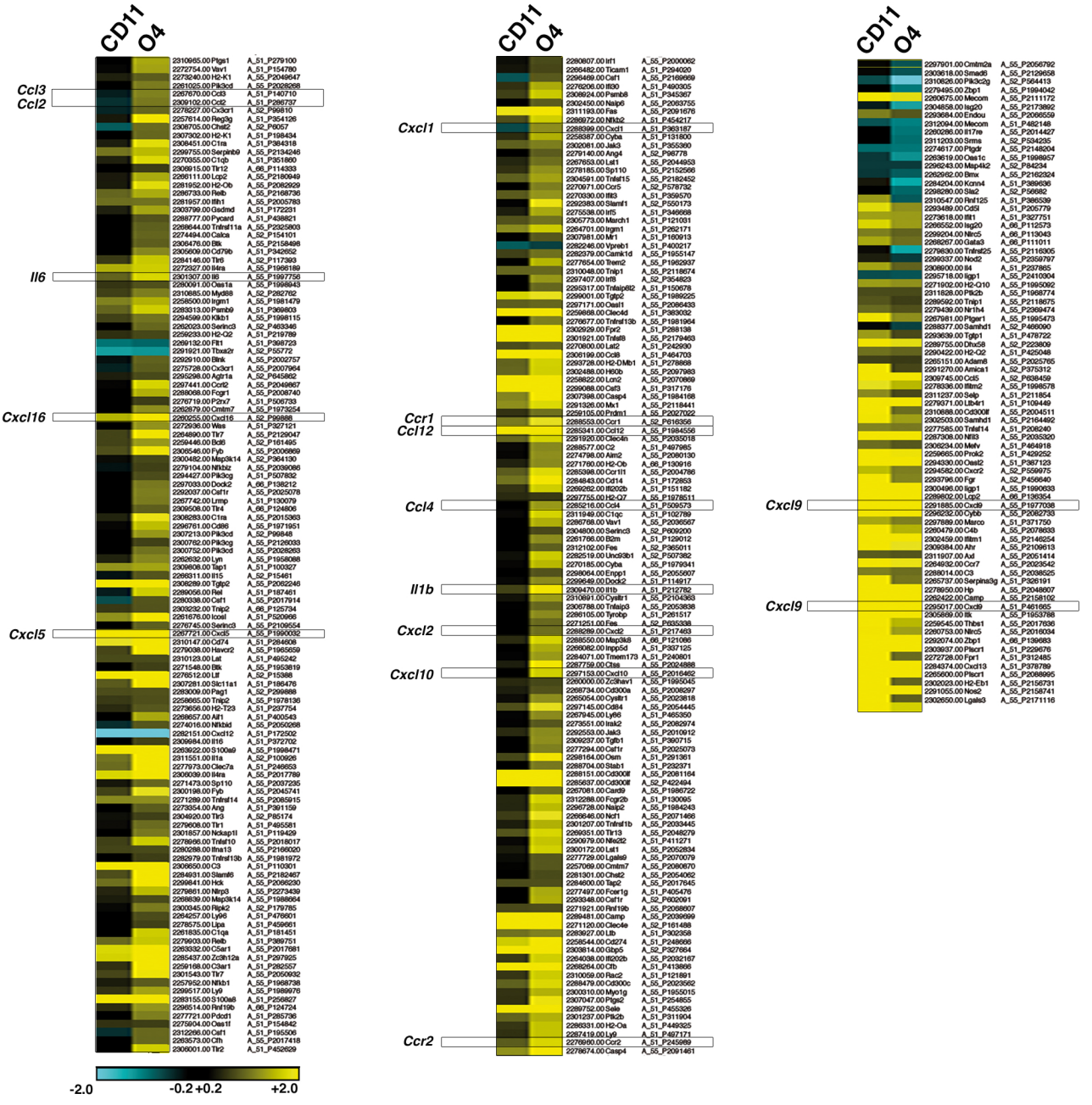
CD11
O4
Ccl3
Ccl2
Il6
Cxcl16
Cxcl5
Cxcl1
Ccr1
Ccl12
Ccl4
Il1b
Cxcl2
Cxcl10
Ccr2
Cxcl9
Cxcl9
-2.0
-0.2 +0.2
+2.0

Figure 5

A

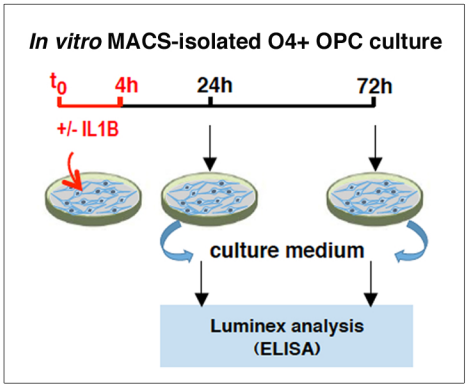
In vitro MACS-isolated O4+ OPC culture
t_0
4h
24h
72h
+/- IL1B
culture medium
Luminex analysis
(ELISA)

B

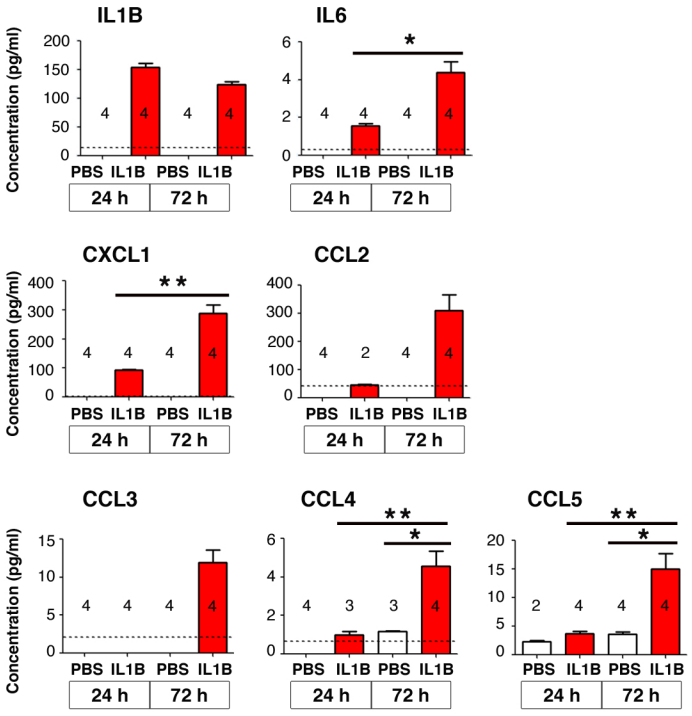
IL1B
IL6
CXCL1
CCL2
CCL3
CCL4
CCL5
Concentration (pg/ml)
PBS IL1B PBS IL1B
24 h
72 h
*
**

Figure S5

A

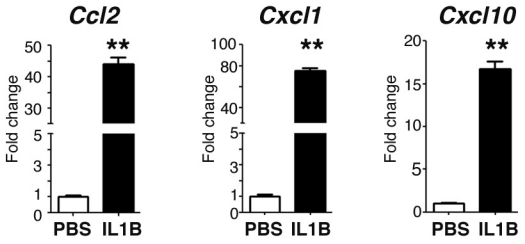

B

ALL

Rank	Motif	Name	P-value	log P-pvalue	q-value (Benjamini)	# Target Sequences with Motif	% of Targets Sequences with Motif	# Background Sequences with Motif	% of Background Sequences with Motif
1		**ISRE**(IRF)/ThioMac-LPS-Expression(GSE23622)/Homer	1,00E-08	-1.915e+01	0.0000	83.0	2.67%	492.7	1.33%
2		**IRF1**(IRF)/PBMC-IRF1-ChIP-Seq(GSE43036)/Homer	1,00E-06	-1.452e+01	0.0001	147.0	4.73%	1148.0	3.09%
3	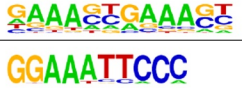	**IRF2**(IRF)/Erythroblas-IRF2-ChIP-Seq(GSE36985)/Homer	1,00E-05	-1.343e+01	0.0002	129.0	4.15%	996.4	2.68%
4		**NFkB-p65-Rel**(RHD)/ThioMac-LPS-Expression(GSE23622)/Homer	1,00E-04	-9.613e+00	0.0065	73.0	2.35%	538.6	1.45%
5		**PGR**(NR)/EndoStromal-PGR-ChIP-Seq(GSE69539)/Homer	1,00E-03	-7.792e+00	0.0320	174.0	5.60%	1604.2	4.31%
6		**NFkB-p65**(RHD)/GM12787-p65-ChIP-Seq(GSE19485)/Homer	1,00E-02	-5.940e+00	0.1698	481.0	15.47%	5097.2	13.71%
7	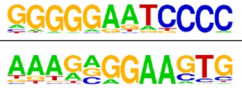	**GRE**(NR),IR3/A549-GR-ChIP-Seq(GSE32465)/Homer	1,00E-02	-5.585e+00	0.2075	133.0	4.28%	1252.3	3.37%
8		**NFkB-p50,p52**(RHD)/Monocyte-p50-ChIP-Chip(Schreiber_et_al.)/Homer	1,00E-02	-5.013e+00	0.3219	178.0	5.73%	1763.5	4.74%
9	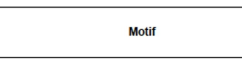	**SpiB**(ETS)/OCILY3-SPIB-ChIP-Seq(GSE56857)/Homer	1,00E-02	-4.708e+00	0.3880	230.0	7.40%	2353.2	6.33%

C

UP

Rank	Motif	Name	P-value	log P-pvalue	q-value (Benjamini)	# Target Sequences with Motif	% of Targets Sequences with Motif	# Background Sequences with Motif	% of Background Sequences with Motif
1		**ISRE**(IRF)/ThioMac-LPS-Expression(GSE23622)/Homer	1,00E-11	-2.571e+01	0.0000	72.0	3.29%	502.8	1.32%
2	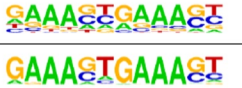	**IRF2**(IRF)/Erythroblas-IRF2-ChIP-Seq(GSE36985)/Homer	1,00E-09	-2.133e+01	0.0000	109.0	4.98%	1002.9	2.63%
3		**IRF1**(IRF)/PBMC-IRF1-ChIP-Seq(GSE43036)/Homer	1,00E-08	-1.892e+01	0.0000	118.0	5.39%	1166.3	3.06%
4		**NFkB-p65-Rel**(RHD)/ThioMac-LPS-Expression(GSE23622)/Homer	1,00E-04	-1.076e+01	0.0021	57.0	2.61%	546.2	1.43%
5		**PGR**(NR)/EndoStromal-PGR-ChIP-Seq(GSE69539)/Homer	1,00E-04	-1.001e+01	0.0035	135.0	6.17%	1655.1	4.34%
6		**IRF4**(IRF)/GM12878-IRF4-ChIP-Seq(GSE32465)/Homer	1,00E-03	-8.091e+00	0.0198	246.0	11.24%	3450.0	9.06%
7		**NFkB-p65**(RHD)/GM12787-p65-ChIP-Seq(GSE19485)/Homer	1,00E-03	-7.672e+00	0.0258	349.0	15.95%	5127.7	13.46%
8		**PU.1**(ETS)/ThioMac-PU.1-ChIP-Seq(GSE21512)/Homer	1,00E-03	-7.299e+00	0.0327	346.0	15.81%	5107.0	13.41%
9		**GRE**(NR),IR3/A549-GR-ChIP-Seq(GSE32465)/Homer	1,00E-03	-7.297e+00	0.0327	102.0	4.66%	1274.8	3.35%
10		**SpiB**(ETS)/OCILY3-SPIB-ChIP-Seq(GSE56857)/Homer	1,00E-03	-7.060e+00	0.0332	174.0	7.95%	2381.8	6.25%
11		**T1ISRE**(IRF)/ThioMac-Ifnb-Expression/Homer	1,00E-02	-5.778e+00	0.1089	12.0	0.55%	81.0	0.21%
12		**Jun-AP1**(bZIP)/K562-cJun-ChIP-Seq(GSE31477)/Homer	1,00E-02	-5.586e+00	0.1209	129.0	5.90%	1764.0	4.63%
13	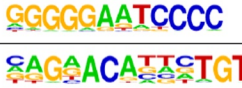	**FOXP1**(Forkhead)/H9-FOXP1-ChIP-Seq(GSE31006)/Homer	1,00E-02	-5.484e+00	0.1236	199.0	9.10%	2874.6	7.55%
14		**Etv2**(ETS)/ES-ER71-ChIP-Seq(GSE59402)/Homer(0.967)	1,00E-02	-5.312e+00	0.1363	616.0	28.15%	9790.6	25.70%
15		**PU.1:IRF8**(ETS:IRF)/pDC-Irf8-ChIP-Seq(GSE66899)/Homer	1,00E-02	-5.274e+00	0.1363	128.0	5.85%	1766.9	4.64%
16		**NFkB-p50,p52**(RHD)/Monocyte-p50-ChIP-Chip(Schreiber_et_al.)/Homer	1,00E-02	-5.184e+00	0.1363	126.0	5.76%	1740.2	4.57%
17		**GRE**(NR),IR3/RAW264.7-GRE-ChIP-Seq(Unpublished)/Homer	1,00E-02	-4.809e+00	0.1857	147.0	6.72%	2093.4	5.50%
18		**ARE**(NR)/LNCAP-AR-ChIP-Seq(GSE27824)/Homer	1,00E-02	-4.777e+00	0.1857	170.0	7.77%	2461.1	6.46%

Figure 6

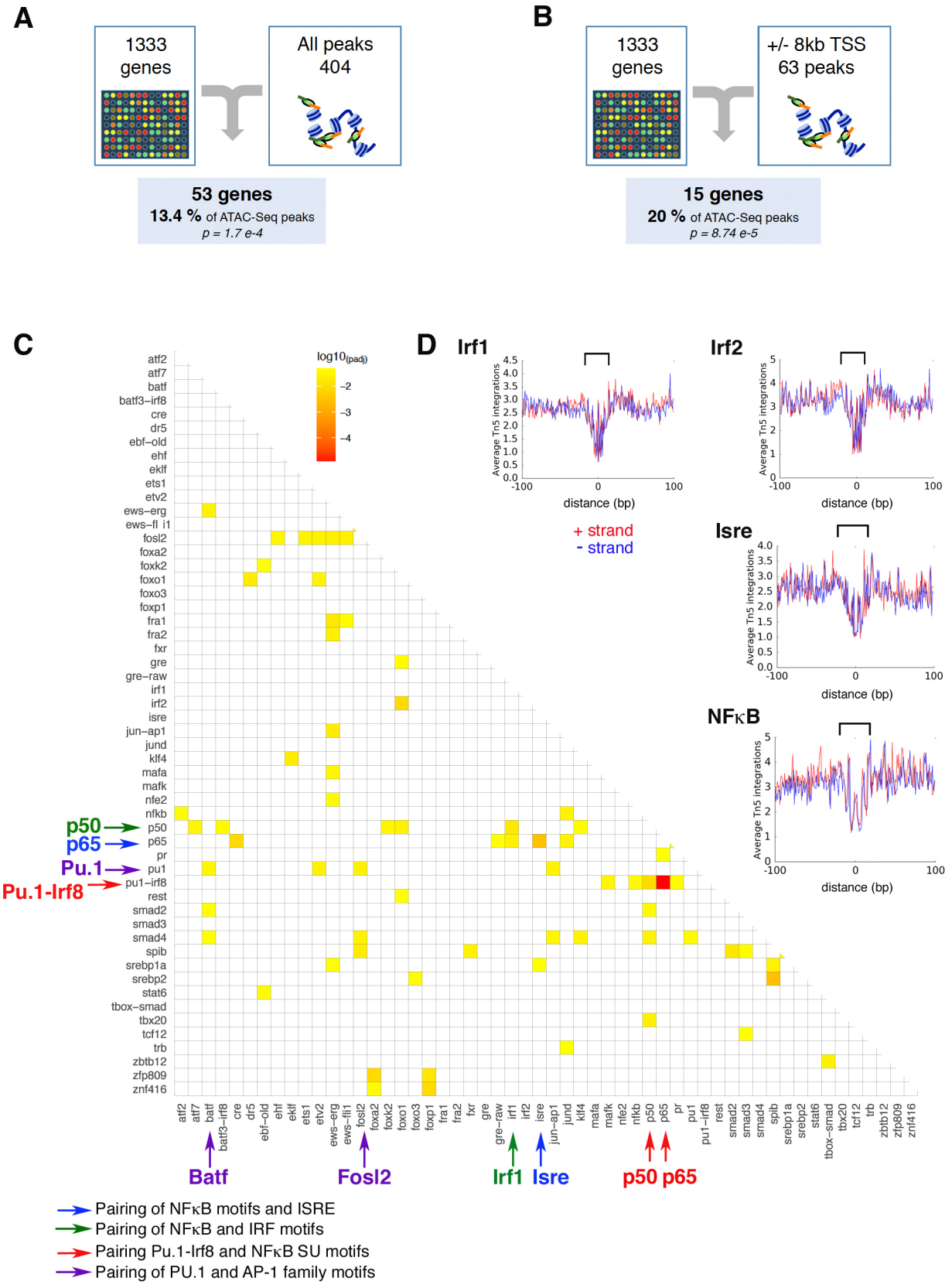
A
1333 genes
All peaks 404
53 genes
13.4 % of ATAC-Seq peaks
p = 1.7 e-4
B
1333 genes
+/- 8kb TSS 63 peaks
15 genes
20 % of ATAC-Seq peaks
p = 8.74 e-5
C
log10(padj)
−2
−3
−4
atf2
atf7
batf
batf3–irf8
cre
dr5
ebf–old
ehf
eklf
ets1
etv2
ews–erg
ews–fli1
fosl2
foxa2
foxk2
foxo1
foxo3
foxp1
fra1
fra2
fxr
gre
gre–raw
irf1
irf2
isre
jun–ap1
jund
klf4
mafa
mafk
nfe2
nfkb
p50
p65
pr
pu1
pu1–irf8
rest
smad2
smad3
smad4
spib
srebp1a
srebp2
stat6
tbox–smad
tbx20
tcf12
trb
zbtb12
zfp809
znf416
p50
p65
Pu.1
Pu.1-Irf8
Batf
Fosl2
Irf1
Isre
p50 p65
D
Irf1
Irf2
Isre
NFκB
Average Tn5 integrations
distance (bp)
+ strand
- strand
Pairing of NFκB motifs and ISRE
Pairing of NFκB and IRF motifs
Pairing Pu.1-Irf8 and NFκB SU motifs
Pairing of PU.1 and AP-1 family motifs

Figure S6

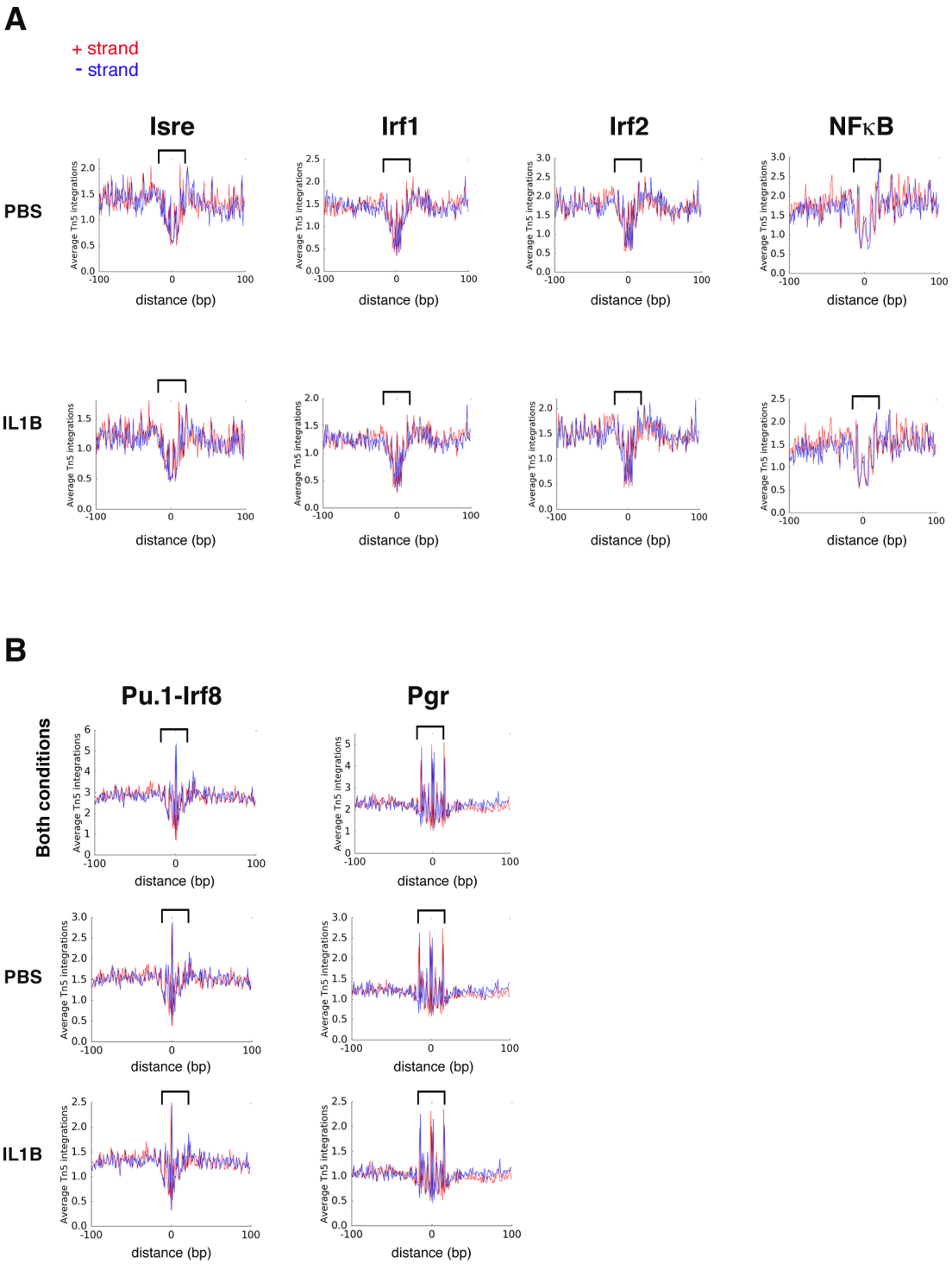
A
+ strand
- strand
Isre
Irf1
Irf2
NFκB
PBS
IL1B
Average Tn5 integrations
distance (bp)
B
Pu.1-Irf8
Pgr
Both conditions
PBS
IL1B
Average Tn5 integrations
distance (bp)

Figure 7

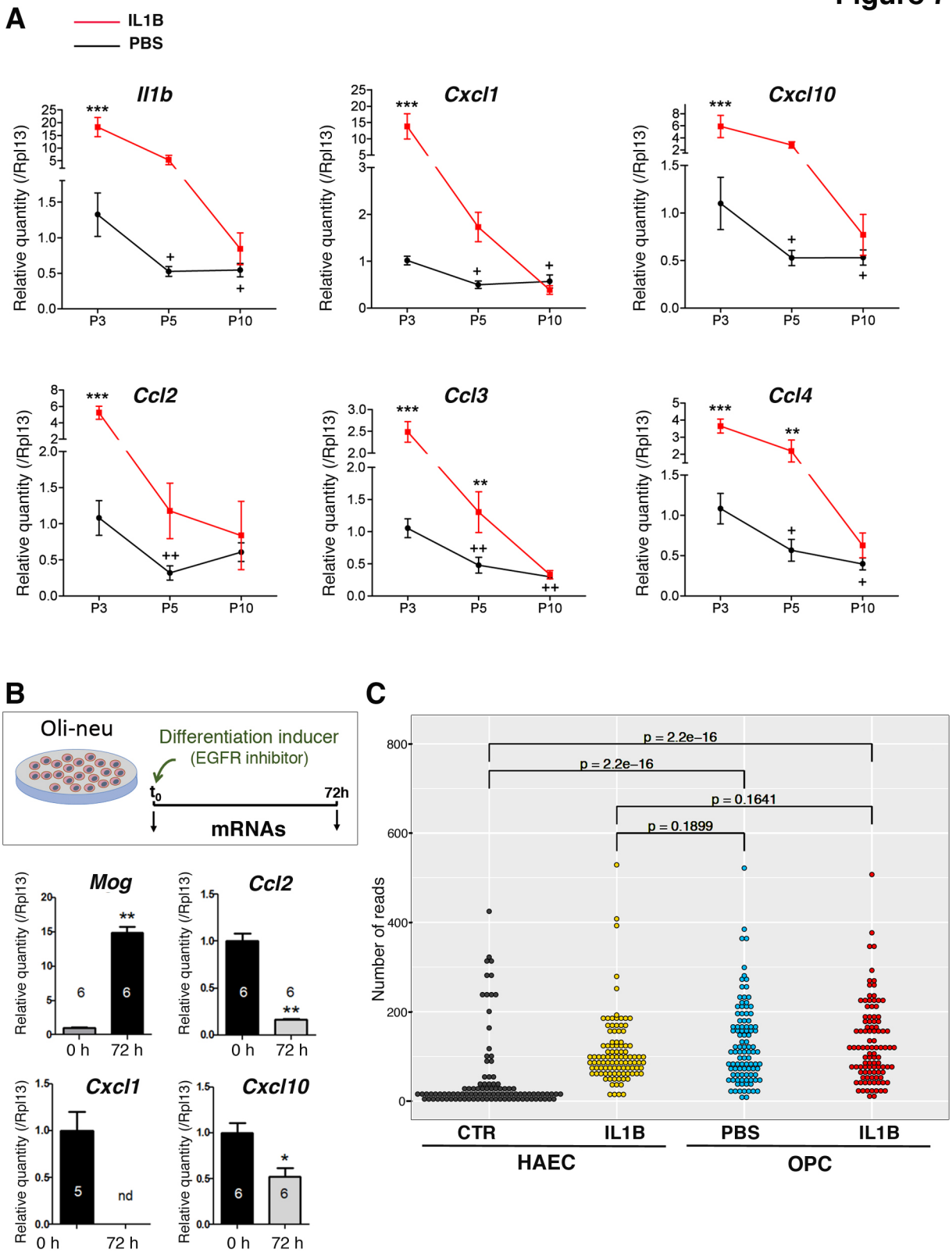
A
IL1B
PBS
Il1b
Cxcl1
Cxcl10
Ccl2
Ccl3
Ccl4
Relative quantity (/Rpl13)
P3
P5
P10
B
Oli-neu
Differentiation inducer
(EGFR inhibitor)
t0
72h
mRNAs
Mog
Ccl2
Cxcl1
Cxcl10
0 h
72 h
nd
C
p = 2.2e−16
p = 2.2e−16
p = 0.1641
p = 0.1899
Number of reads
CTR
IL1B
PBS
IL1B
HAEC
OPC

Figure S7

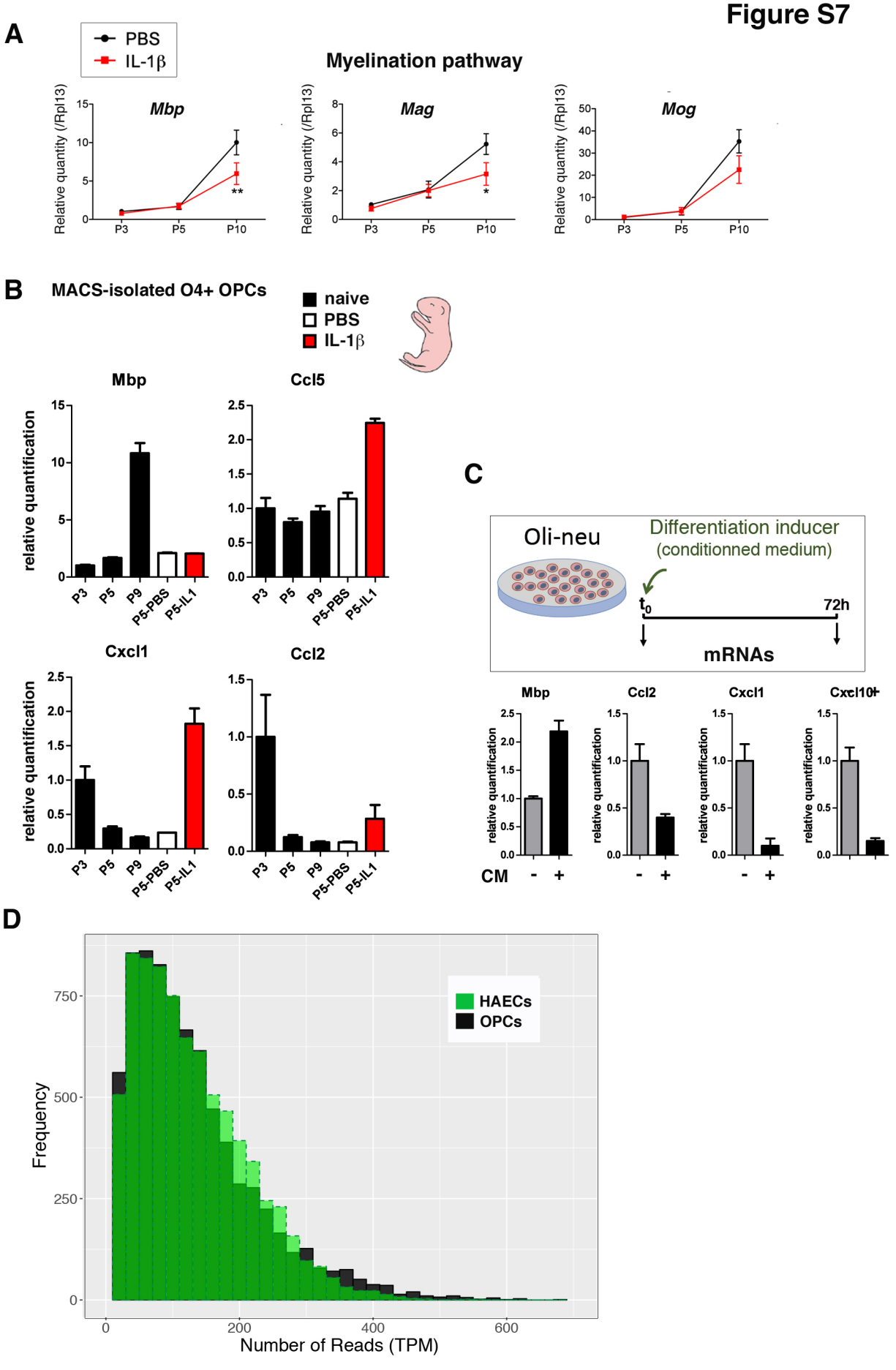
A
PBS
IL-1β
Myelination pathway
Mbp
Mag
Mog
Relative quantity (/Rpl13)
P3
P5
P10
B
MACS-isolated O4+ OPCs
naive
PBS
IL-1β
Mbp
Ccl5
Cxcl1
Ccl2
relative quantification
P3
P5
P9
P5-PBS
P5-IL1
C
Oli-neu
Differentiation inducer
(conditionned medium)
t0
72h
mRNAs
Mbp
Ccl2
Cxcl1
Cxcl10
relative quantification
CM
D
HAECs
OPCs
Frequency
Number of Reads (TPM)

Table S1. Alignment Statistics of ATAC-Seq data

Paired		PBS1	PBS2	PBS3	IL1B1	IL1B2	IL1B3
Total Reads		73 686 516	67 049 336	79 305 947	74 117 441	61 622 256	76 360 806
Removing Mitochondria	**Remaining Reads**	66 505 362	60 228 153	71 141 195	66 632 160	55 217 126	66 962 284
	% of Total Removed	9.75%	10.17%	10.30%	10.10%	10.39%	12.31%
% Reads Remaining to Align to Nuclear		90.25%	89.83%	89.70%	89.90%	89.61%	87.69%
Nuclear Only	**Con 1 time only**	57 751 458	52 192 349	62 471 914	56 958 297	47 542 920	58 362 195
	Con >1 time	340 054	325 951	371 952	348 211	320 270	351 148
	Discon 1 time	47 160	34 979	42 034	43 352	31 631	39 905
	Without mates 1	541 607	526 165	592 143	522 936	491 098	569 201
	Without mates >1	340 054	325 951	371 952	348 211	320 270	351 148
	Total All Alignments	*59 020 333*	*53 405 395*	*63 849 995*	*58 221 007*	*48 706 189*	*59 673 597*
	% of total reads	80.10%	79.65%	80.51%	78.55%	79.04%	78.15%

Nuclear Reads Mapping 1 time only	58 340 225	52 753 493	63 106 091	57 524 585	48 065 649	58 971 301

% of Total Reads Mapping to nucleus 1 time only	79.17%	78.68%	79.57%	77.61%	78.00%	77.23%

The alignment statistics of the samples is in line with what are expected from ATAC-seq samples. Losing in the region of 10% of reads to mitochondrial alignment is usual for this type of data.

	Forward	Reverse
Ccl2	CATCCACGTGTTGGCTCA	TCATTGGGATCATCTTGCTG
Ccl3	TTTTGAAACCAGCAGCCTTT	CTGCCTCCAAGACTCTCAGG
Ccl4	CCCACTTCCTGCTGTTTCTC	GTCTGCCTCTTTTGGTCAGG
Ccl5	GTGCCCACGTCAAGGAGTAT	CCCACTTCTTCTCTGGGTTG
Ccr1	AGGCCCAGAAACAAAGTCTG	TTGTGGGGTAGGCTTCTGTG
Ccr2	GCCAGGACAGTTACCTTTGG	TTCCTGGTAGAGAGGCAAACA
Cnp	AGACAGCGTGGCGACTAGACT	GGGCTTCAGCTTCTTCAGGT
Cxcl1	GCACCCAAACCGAAGTCATA	AGGTGCCATCAGAGCAGTCT
Cxcl10	GCTGCAACTGCATCCATATC	GGATTCAGACATCTCTGCTCAT
Cxcl12	AGAGCCAACGTCAAGCATCT	TAATTTCGGGTCAATGCACA
Cxcl13	GGAGAGCGACACAGCAGAAC	ACCACCTCTCCCATGTCATC
Cxcl16	GGAGAGCGACACAGCAGAAC	ACCACCTCTCCCATGTCATC
Cxcl2	CAAGGGCGGTCAAAAAGTT	TCCAGGTCAGTTAGCCTTGC
Cxcl9	ACGGAGATCAAACCTGCCTA	TTTCCCCCTCTTTTGCTTTT
Gapdh	GGCCTTCCGTGTTCCTAC	TGTCATCATACTTGGCAGGTT
Gfap	AAGCCAAGCACGAAGCTAAC	CTCCTGGTAACTGGCCGACT
Id2	CTGGACTCGCATCCCACTAT	CGACATAAGCTCAGAAGGGAAT
Il1a	GACGGCTGAGTTTCAGTGAG	TAAGGTGCTGATCTGGGTTG
Il1b	GGGCCTCAAAGGAAAGATTC	TCTTCTTTGGGTATTGCTTGG
Il1r1	CAAGCTGTTCATTTATGGAAGG	ATCAGCCTCCTGCTTTTCTTT
Il1r2	TAAATGTGTTGCCTCGAATCC	CTCCAGGAGAACGTGGAAGA
Il6	CAAAGCCAGAGTCCTTCAGA	GCCACTCCTTCTGTGACTCC
Il6ra	CGTTTGGGTTGCTTCTCTGT	GTGGAGGAGAGGTCGTCTTG
Itgam	CTGGTGCTCTTGGCTCTCAT	GGCAGCTTCATTCATCATGT
Mbp	CCGGACCCAAGATGAAAAC	CTTGGGATGGAGGTGGTGT
Mog	AAGAGGCAGCAATGGAGTTG	GACCTGCAGGAGGATCGTAG
Pdgfra	GACGTTCAAGACCAGCGAGTT	CAGTCTGGCGTGCGTCC
Rbfox3(NeuN)	CAGATATGCTCAGCCAGCAG	CGATGCTGTAGGTTGCTGTG
Rpl13a	ACAGCCACTCTGGAGGAGAA	GAGTCCGTTGGTCTTGAGGA